Chapter 3. A Novel Magneto-Thermoelastic Constitutive Model

3.1. Introduction

A comprehensive generalized coupled magneto-thermo-elastic nonlinear hysteretic constitutive model is aimed to develop in this chapter in order to determine the performance and in-service strength of magnetostrictive devices more accurately. This three-dimensional vector model is not only applicable to a wide range of stress and magnetic field, including the physics of demagnetization and Weiss molecular field, but also it works efficiently even in the presence of simultaneous application of the three-dimensional magnetic field. This chapter aims to propose a thermodynamically motivated constitutive description that can precisely quantify the inherent vectorial hysteretic nature of magnetization and magneto-strain in three dimensions, stress anisotropies for both small and large prestress levels and temperature effects along with the contribution of demagnetizing field and Weiss molecular field. A Gibbs free energy density function for elastic deformation is combined with thermodynamic relations to establish a framework for coupled field polynomial constitutive relations. According to magnetic domain theory [39], the elastic strain caused by various prestresses is decomposed into linear elastic strain and nonlinear elastic strain arising due to the magnetic domain rotations. Further, the nonlinear part of elastic strain for macroscopic bulk materials is estimated by a vector function of the hyperbolic tangent, i.e. based on the knowledge of isotropic elasticity theory and the physical facts for magnetostrictive volumetric strain[4]. In addition, the thermal strain is also split in thermal expansion and coupled thermo-magnetic strain [104]. More robust estimate, which is the vector generalization approach for the J-A model to three dimensions, is used for capturing the magnetic hysteresis effects [105]. Based on the strong physical and experimental background, the scalar Langevin function [50,106] (derived from Boltzmann statistics) has

been used to represent the anhysteretic magnetization. In order to improve the magnetization vector representation, Leite et al. [107] suggested a vector version of Langevin function $f(\boldsymbol{x}) = [coth\,(|\boldsymbol{x}|) - 1/|\boldsymbol{x}|](\boldsymbol{x}/|\boldsymbol{x}|)$ that retains both the physical nature of Langevin function and also adequately depicts the anhysteretic magnetization vector. A coupling of the nonlinear magneto-thermo-elastic phenomenon along with hysteresis behavior on physical basis of giant magnetostrictive material is eventually accomplished to obtain a concise hysteretic constitutive description. This fully coupled hysteretic constitutive description along with the governing equations of magnetic field, elastic field, and thermal field is solved numerically in COMSOL Multiphysics. The simulated numerical results demonstrate that this constitutive description can efficiently capture the effect of demagnetizing field and Weiss molecular field on the nonlinear characteristics of magnetostrictive rods and films and hence contribute further to the understanding and design of magnetostrictive smart devices. Moreover, this model can fully describe the combined effect of prestress, temperature and applied magnetic field on the magnetostriction, magnetization and elastic strain inclusive of the ΔE effect.

3.2. Coupled Nonlinear Hysteretic Constitutive Relationship

Giant magnetostrictive materials (e.g., Terfenol-D) usually have practical applications in the form of rods, bars, and films. In addition to that, they are subjected to external excitations (such as applied magnetic field and prestresses) at ambient temperature. Thus, the response of the giant magnetostrictive materials primarily rely on the exchange interaction energy (E^{ex}) between the domains, the magneto-static energy as demagnetization energy (E^{d}), the magnetization (M_k), the pre-stresses (σ_{ij}) and the temperature (T). The Weiss' molecular field provides an approximate representation of the exchange interaction energy of quantum mechanics [4].

3.2.1. Mathematical framework

Consider a giant magnetostrictive material subjected to the three-dimensional stress state and placed under the effect of an externally applied magnetic field. A coupled field polynomial constitutive relationship between magnetization (M_k), applied magnetic field (H_k), stress (σ_{ij}), strain (ε_{ij}) and temperature (T) can be established from the Gibbs free energy density function for elastic deformation combined with thermodynamic relations. The Gibbs free energy density function for elastic deformation is defined as[108]

$$G(\sigma_{ij}, M_k, T) = U - TS - \sigma_{ij}\varepsilon_{ij} \tag{3.1}$$

where U is the internal energy density of magnetostrictive material, T is the absolute temperature, and S is entropy.

Further, incorporating the contribution of the exchange interaction energy density (E^{ex}) from Eq. (2.5) and the demagnetization energy density (E^{d}) from Eq. (2.7), the derivative of the internal energy density can be written analogous to [108]

$$dU = \sigma_{ij}d\varepsilon_{ij} + \mu_o H_k dM_k + \mu_o \eta' \delta_{kl} M_k dM_k - \mu_o N_{kl} M_k dM_k + TdS \tag{3.2}$$

Thus, after calculating the total differential of eq. (2) and substituting the value of the differential of the internal energy density function, we get

$$dG = -\varepsilon_{ij}d\sigma_{ij} + \mu_o H_k dM_k + \mu_o \eta' \delta_{kl} M_k dM_k - \mu_o N_{kl} M_k dM_k - SdT \tag{3.3}$$

Then, one can deduce the following thermodynamic relations [109]

$$\mu_o H_k + \mu_o \eta' \delta_{kl} M_k - \mu_o N_{kl} M_k = \frac{\partial G}{\partial M_k}, \quad \varepsilon_{ij} = -\frac{\partial G}{\partial \sigma_{ij}}, \qquad and \quad S = \frac{\partial G}{\partial T} \tag{3.4}$$

In order to derive polynomial constitutive relations, the Gibbs free energy density function $G(\sigma_{ij}, M_k, T)$ can be expanded by a Taylor series expansion about reference

point $(\sigma_{ij}, M_k, T) = (0, 0, T_r)$. Here, T_r is easy axis transition temperature at free state which is usually 0^oC for Terfenol-D[110]. Therefore in the present work, the coupled magneto-strain behaviour of the magnetostrictive material above the easy axis transition temperature (i.e. near room temperature) is mainly considered[111]. Then we can obtain the polynomial forms of strain ε_{ij} and magnetic field H_k as described in Eq. (5). Based on the above discussion and some recent theories presented by Zheng et al[39,41,77], the constitutive relations in tensor form with indices i, j, k, l, m, n are expressed in the following form:

$$\varepsilon_{ij} = \underbrace{-\left(\frac{\partial^2 G}{\partial\sigma_{ij}\partial\sigma_{kl}} + \frac{1}{2}\frac{\partial^3 G}{\partial\sigma_{ij}\partial\sigma_{kl}\partial\sigma_{mn}}\sigma_{mn} + \ldots..\right)\sigma_{kl}}_{\varepsilon_{ij}^{I}(\sigma_{kl})} \tag{3.5}$$

$$\underbrace{-\frac{1}{2}\left(\frac{\partial^3 G}{\partial\sigma_{ij}\partial M_k\partial M_l} + \frac{1}{2}\frac{\partial^5 G}{\partial\sigma_{ij}\partial M_k\partial M_l\partial T^2}\Delta T^2 + \ldots + \frac{\partial^4 G}{\partial\sigma_{ij}\partial\sigma_{mn}\partial M_k\partial M_l}\sigma_{mn} + \frac{\partial^5 G}{\partial\sigma_{ij}\partial\sigma_{mn}\partial M_k\partial M_l\partial T}\sigma_{mn}\Delta T \ldots\right)M_k M_l}_{\varepsilon_{ij}^{II}(M_k,\sigma_{mn},T)}$$

$$\underbrace{-\frac{\partial^2 G}{\partial T\partial\sigma_{ij}}\Delta T + \ldots..}_{\varepsilon_{ij}^{III}(\sigma_{mn},T)} \underbrace{-\frac{1}{2}\frac{\partial^4 G}{\partial\sigma_{ij}\partial T\partial M_k\partial M_l}M_k M_l\Delta T + \ldots}_{\varepsilon_{ij}^{IV}(M_k,\sigma_{mn},T)}$$

$$H_k + \eta'\delta_{kl}M_k - \mu_o N_{kl}M_k = \underbrace{\frac{1}{\mu_o}\left(\frac{\partial^2 G}{\partial M_k\partial M_l} + \frac{1}{3!}\frac{\partial^4 G}{\partial M_k\partial M_l\partial M_i\partial M_j}M_i M_j + \ldots. + \frac{\partial^3 G}{\partial T\partial M_k\partial M_l}\Delta T \ldots\ldots\ldots\right)M_l}_{H_k^{I}(M_l,T)} \tag{3.6}$$

$$\underbrace{+\frac{1}{\mu_o}\left(\frac{\partial^3 G}{\partial\sigma_{ij}\partial M_k\partial M_l} + \frac{1}{2}\frac{\partial^5 G}{\partial\sigma_{ij}\partial M_k\partial M_l\partial T^2}\Delta T^2 + \ldots.. + \frac{1}{2}\frac{\partial^4 G}{\partial\sigma_{ij}\partial\sigma_{mn}\partial M_k\partial M_l}\sigma_{mn} + \frac{1}{2}\frac{\partial^5 G}{\partial\sigma_{ij}\partial\sigma_{mn}\partial M_k\partial M_l\partial T}\sigma_{mn}\Delta T \ldots.\right)\sigma_{ij}M_l + \ldots}_{H_k^{II}(M_l,\sigma_{mn},T)}$$

$$\underbrace{+\frac{1}{\mu_o}\left(\frac{\partial^4 G}{\partial\sigma_{ij}\partial T\partial M_k\partial M_l}\ldots\ldots\ldots\right)\Delta T\sigma_{ij}M_l + \ldots}_{H_k^{III}(M_l,\sigma_{mn},T)}$$

As illustrated in Eq. (3.5), the strain parameter ε_{ij} is separated into four components, namely $\varepsilon_{ij}^{I}(\sigma_{kl})$, $\varepsilon_{ij}^{II}(M_k, \sigma_{mn}, T)$, $\varepsilon_{ij}^{III}(\sigma_{mn}, T)$, and $\varepsilon_{ij}^{IV}(M_k, \sigma_{mn}, T)$.

The first part of the strain $\varepsilon_{ij}^{I}(\sigma_{kl})$ is caused by applied stress alone. The applied pre-stress changes the orientation of magnetic domains parallel to a plane perpendicular to the axial direction of magnetostrictive material. This induces pre-compression due to the rotation of magnetic domains before a magnetic field is applied. This process exhibits saturation phenomenon [4] at pre-stress level (σ_s) known as saturation stress indicated by the

completion of rotation of all the magnetic domains. After the saturation stress, with an increment in stress level, the developed strain is the elastic strain. Hence, when high enough magnetic field is applied along the axis of pre-stressed magnetostrictive material, a higher relative magnetostrictive strain is obtained. Thus, strain $\varepsilon_{ij}^{I}(\sigma_{kl})$ can be split in a part independent of domain rotation and another part dependent on domain rotation. The part independent of domain rotation is linear with respect to stress σ_{kl} which can be described by a conventional compliance tensor S_{ijkl} and the latter is nonlinear, which can be described by a nonlinear function $\lambda_{0ij}(\sigma_{mn})$. Hence

$$\varepsilon_{ij}^{I}(\sigma_{kl}) = S_{ijkl}\sigma_{kl} + \lambda_{0ij}(\sigma_{mn}) \tag{3.7}$$

Now, the magnetostrictive strain $\varepsilon_{ij}^{II}(M_k, \sigma_{mn}, T)$ in Eq. (3.5) is concerned with the coupled magneto-thermo-elastic response. The value of magnetostrictive strain is zero before the material is magnetized and attains its maximum value depending on pre-stress and ambient temperature when the magnetization of material reaches towards saturation $M_s(T)$. According to preceding analysis, it is evident that pre-stress is responsible for pre-contraction $\lambda_{0ij}(\sigma_{mn})$ due to the rotation of magnetic domains and vice versa. Therefore, changes in maximum magnetostriction due to pre-stress will be equal to $-\lambda_{0ij}(\sigma_{mn})$. A fourth-order magnetostrictive tensor m_{ijkl} is used to define free magnetostrictive-strain at stress-free state [37]. Thus, m_{ijkl} represents the proportionality factors between the induced magnetostrictive strains and the applied magnetic field. Invoking the experimental results of Clark [5], only quadratic magnetization terms are considered as coupling terms. According to ferromagnetic theory [112],[42], if $\Delta T = T - T_r$ is the difference between ambient and the easy axis transformation temperature T_r, T_c is the curie temperature and M_s is saturation magnetization value of the easy axis transformation temperature T_r, then saturation magnetization at ambient temperature can be evaluated as

$$M_s(T) = M_s\left(1 - \frac{\Delta T}{T_c - T_r}\right)^{\gamma} \tag{3.8}$$

where amplification coefficient γ reflects the slope of change in saturation magnetization with temperature; the smaller value of γ means more slowly the $M_s(T)$ changes with temperature. For Terfenol-D, $T_r = 0℃$, $T_c = 383.3℃$ and $\gamma = 0.78$ [42].

Presently, the dependence of strain terms $\varepsilon_{ij}^{II}(M_k, \sigma_{mn}, T)$ on the quadratic magnetization is expressed in a general form analogous to Jin, et al[54] as:

$$\begin{aligned}
&\varepsilon_{ij}^{II}(M_k, \sigma_{mn}, T) \qquad (3.9)\\
&= -\frac{1}{2}\left(\frac{\partial^3 G}{\partial\sigma_{ij}\partial M_k\partial M_l} + \frac{1}{2}\frac{\partial^5 G}{\partial\sigma_{ij}\partial M_k\partial M_l\partial T^2}\Delta T^2 + \cdots\right.\\
&+ \frac{\partial^4 G}{\partial\sigma_{ij}\partial\sigma_{mn}\partial M_k\partial M_l}\sigma_{mn}\\
&\left.+ \frac{\partial^5 G}{\partial\sigma_{ij}\partial\sigma_{mn}\partial M_k\partial M_l\partial T}\sigma_{mn}\Delta T \ldots\right) M_k M_l\\
&= \left[m_{ijkl} - \frac{\lambda_{0ij}(\sigma_{mn})}{(M_s(T))^2}\delta_{kl}\right] M_k M_l
\end{aligned}$$

The temperature-dependent strain $\varepsilon_{ij}^{III}(\sigma_{mn}, T)$ is caused by thermal expansion of material and directly proportional to the change in temperature. Thus, it can be expressed by introducing an isotropic coefficient of thermal expansion $(\alpha_{ij} = \alpha\delta_{ij})$ as [113]

$$\varepsilon_{ij}^{III}(\sigma_{mn}, T) = \alpha\delta_{ij}\Delta T \tag{3.10}$$

The fourth part strain term $\varepsilon_{ij}^{IV}(M_k, \sigma_{mn}, T)$ shows the thermo-magnetic coupling. The experimental results of Clark[104] indicate that the saturation magnetostrictive strain exhibits a linearly decreasing trend with increasing temperature above the easy axis

transition temperature, T_r. If the linear variation coefficient in the isotropic case is set as $\beta_{ij} = \beta\delta_{ij}$, then the strain term $\varepsilon_{ij}^{IV}(M_k, \sigma_{mn}, T)$ can be expressed as

$$\varepsilon_{ij}^{IV}(M_k, \sigma_{mn}, T) = \frac{\beta\delta_{ij}}{(M_s(T))^2}\Delta T M_k M_l \delta_{kl} \tag{3.11}$$

The functional parameters of the Eq.(3.6) is divided into three components with reference to their respective dependency as $H_k^I(M_l, T)$, $H_k^{II}(M_l, \sigma_{mn}, T)$ and $H_k^{III}(M_l, \sigma_{mn}, T)$.

The first part of the magnetic field $H_k^I(M_l, T)$ is independent of stress and exhibits the stress-free magnetization relationship as $M_l = M_s(T)f(k(T)H_k)$. Since the behaviour of material saturation trend is nonlinear, hence an inverse nonlinear vector function $f_k^{-1}(M_l)$ should be adopted to define the relationship. Therefore,

$$H_k^I(M_l) = f_k^{-1}(M_l) \tag{3.12}$$

The coupled part of the magnetic field $H_k^{II}(M_l, \sigma_{mn}, T)$ shows the effect of pre-stress on the magnetization of the material at ambient temperature. With the help of Eq. (3.5) and Eq. (3.9), $H_k^{II}(M_l, \sigma_{mn}, T)$ can be expressed as:

$$\begin{aligned} & H_k^{II}(M_l, \sigma_{mn}, T) \qquad (3.13) \\ & = \frac{1}{\mu_o}\left[\frac{1}{2}\left(\frac{\partial^3 G}{\partial\sigma_{ij}\partial M_k\partial M_l} + \frac{1}{2}\frac{\partial^5 G}{\partial\sigma_{ij}\partial M_k\partial M_l\partial T^2}\Delta T^2 + \cdots\right.\right. \\ & + \frac{\partial^4 G}{\partial\sigma_{ij}\partial\sigma_{mn}\partial M_k\partial M_l}\sigma_{mn} \\ & \left. + \frac{\partial^5 G}{\partial\sigma_{ij}\partial\sigma_{mn}\partial M_k\partial M_l\partial T}\sigma_{mn}\Delta T \ldots\right)\sigma_{ij}M_l \\ & \left. + \frac{1}{2}\left(\frac{\partial^3 G}{\partial\sigma_{ij}\partial M_k\partial M_l} + \frac{1}{2}\frac{\partial^5 G}{\partial\sigma_{ij}\partial M_k\partial M_l\partial T^2}\Delta T^2 + \ldots\right)\sigma_{ij}M_l\right] \end{aligned}$$

$$= \frac{1}{\mu_o}\left[-\frac{\varepsilon_{ij}^{II}(M_k,\sigma_{mn},T)}{M_k}\sigma_{ij} - m_{ijkl}\sigma_{ij}M_l\right]$$

$$= -\frac{1}{\mu_o}\left[2m_{ijkl} - \frac{\lambda_{0ij}(\sigma_{mn})}{(M_s(T))^2}\delta_{kl}\right]\sigma_{ij}M_l$$

Referring to Eq.(3.11), the terms related to the inverse magneto-thermo-elastic coupling effect on the magnetic field can be written as

$$H_k^{III}(M_l,\sigma_{mn},T) = -\frac{2}{\mu_o}\left(\frac{\varepsilon_{ij}^{IV}(M_k,\sigma_{mn},T)}{M_k}\sigma_{ij}\right) \tag{3.14}$$

$$= -\frac{2\beta\delta_{ij}}{\mu_o(M_s(T))^2}\Delta T\sigma_{ij}M_l\delta_{kl}$$

Now, ε_{ij}, H_k is expressed in a general form as:

$$\varepsilon_{ij} = S_{ijkl}\sigma_{kl} + \lambda_{0ij}(\sigma_{mn}) + \left[m_{ijkl} - \frac{\lambda_{0ij}(\sigma_{mn})}{(M_s(T))^2}\delta_{kl}\right]M_kM_l + \alpha\delta_{ij}\Delta T \tag{3.15}$$

$$+ \frac{\beta\delta_{ij}}{(M_s(T))^2}\Delta TM_kM_l\delta_{kl}$$

$$H_k = f_k^{-1}(M_l) - \eta'\delta_{kl}M_l + N_{kl}M_l - \frac{1}{\mu_o}\left[2m_{ijkl}\sigma_{ij} - \frac{\lambda_{0ij}(\sigma_{mn})\sigma_{ij}}{\left(M_s(T)\right)^2}\delta_{kl}\right] \tag{3.16}$$

$$- \frac{2\beta\delta_{ij}}{\mu_o(M_s(T))^2}\Delta T\sigma_{ij}M_l\delta_{kl}$$

Equations (3.15) and (3.16) gives the general form of coupled magneto-thermo-elastic constitutive relationship in this paper. Based on physical and experimental observations, the fourth-order tensors and nonlinear functions can be determined.

3.3. Qualitative Discussion

3.3.1. On tensors S_{ijkl} and m_{ijkl}

The compliance tensor has the symmetry properties, therefore considering the isotropic case it can be expressed as [113]

$$S_{ijkl} = \frac{1}{E_{in}}\left[\frac{1}{2}(1+\nu)\left(\delta_{ik}\delta_{jl} + \delta_{il}\delta_{jk}\right) - \nu\delta_{ij}\delta_{kl}\right] \tag{3.17}$$

Then, $S_{ijkl}\sigma_{kl}$ is rewritten as:

$$S_{ijkl}\sigma_{kl} = \frac{1}{E_{in}}\left[(1+\nu)\sigma_{ij} - \nu\sigma_{kk}\delta_{ij}\right] \tag{3.18}$$

Here, E_{in} and ν are the intrinsic Young's modulus of the material at saturation and the Poisson's ratio, respectively.

For an isotropic case, symmetric magnetostrictive tensor m_{ijkl} can be expressed in terms of saturation magnetostrain and temperature dependent saturation magnetization as [37]

$$m_{ijkl} = \frac{\lambda_s}{(M_s(T))^2}\left[\frac{3}{4}\left(\delta_{ik}\delta_{jl} + \delta_{il}\delta_{jk}\right) - \frac{\delta_{ij}\delta_{kl}}{2}\right] \tag{3.19}$$

Then the following expressions are derived

$$m_{ijkl}M_kM_l = \frac{\lambda_s}{(M_s(T))^2}\left[\frac{3}{2}M_iM_j - \frac{1}{2}M_kM_k\delta_{ij}\right] \tag{3.20}$$

$$m_{ijkl}\sigma_{ij} = \frac{\lambda_s}{(M_s(T))^2}\left[\frac{3}{2}\sigma_{kl} - \frac{1}{2}\sigma_{ii}\delta_{kl}\right] = \frac{\lambda_s}{(M_s(T))^2}\tilde{\sigma}_{kl} \tag{3.21}$$

where the effective stress $\tilde{\sigma}_{kl} = \frac{3}{2}\left[\sigma_{kl} - \frac{1}{3}\sigma_{ii}\delta_{kl}\right]$ is $3/2$ times of stress deviator part of the stress tensor. The constants λ_s and $M_s(T)$ are the maximum magnetostriction when pre-stress is zero and the saturation magnetization at temperature T, respectively.

3.3.2. On $\lambda_{0ij}(\sigma_{mn})$ and $f_k^{-1}(M_l)$

It is a very tedious task to propose an exact non-linear function for $\lambda_{0ij}(\sigma_{mn})$, but one can make an approximation based on some physical facts [114] and the primary features of experimental stress-strain curve for Terfenol-D bar under demagnetized state[17,28]. It can be observed that $\lambda_0(\sigma)$ passes through the origin and monotonically increases with stress from $-\infty$ to ∞. Furthermore, for an isotropic positive magnetostrictive material (material having saturation magnetostriction λ_s greater than zero, e.g., Terfenol-D) the value of non-linear function tends to $-\lambda_s/2$ when stress approaches to $-\infty$ and λ_s when stress approaches to ∞. For better understanding, these features of the nonlinear function $\lambda_0(\sigma)$ are qualitatively plotted in **Figure 3.1** A schematic diagram of the nonlinear part of elastic strain (λ_0) vs. the stress (σ) curve for a giant magnetostrictive material.**Figure 3.1**.

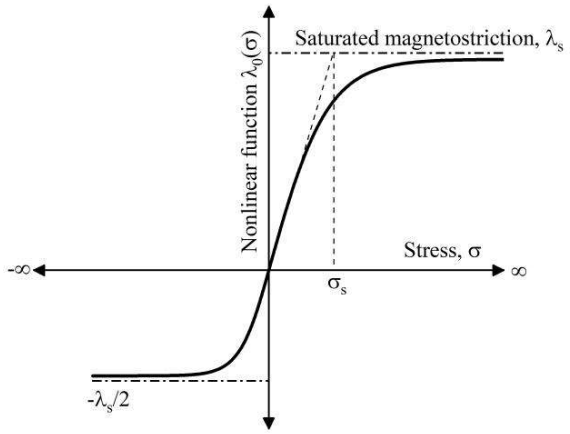

Figure 3.1 A schematic diagram of the nonlinear part of elastic strain (λ_0) vs. the stress (σ) curve for a giant magnetostrictive material.

On the contrary, for negative magnetostrictive material the value of non-linear function tends to λ_s when stress approaches to $-\infty$ and $-\lambda_s/2$ when stress approaches to ∞. Considering the above description of non-linear saturation nature of λ_0, consequently, it is appropriate to choose the hyperbolic tangent function $tanh\ (x)$ for approximation as[39]

$$\lambda_0 = \begin{cases} \lambda_s \tanh\left(\frac{\sigma}{\sigma_s}\right) & \sigma \geq 0 \\ \frac{\lambda_s}{2} \tanh\left(\frac{2\sigma}{\sigma_s}\right) & \sigma < 0 \end{cases} \tag{3.22}$$

The volume of a magnetostrictive material remains fairly constant between the demagnetized state and saturation magnetization [4] (due to domain rotations). Therefore, the transverse magnetostriction in 3-D Cartesian coordinate system $O - x, y, z,$ should always be one half of the longitudinal magnetostriction in the opposite sign, and volumetric strain due to magnetostriction becomes zero, i.e., $\lambda_{0xx} + \lambda_{0yy} + \lambda_{0zz} = 0$. So, if saturation stress (σ_s) for domain rotations is applied in the longitudinal direction (say z-direction) causing pre-compression $\lambda_{0zz} = -\lambda_s/2$ then one can obtain $\lambda_{0xx} = \lambda_{0yy} = \lambda_s/4$. From the knowledge of elasticity theory, for the 3-D case with multi-axial loading, it is noted that the effective stress $\tilde{\sigma}_{kl}$ is solely responsible for strain component $\lambda_{0ij}(\sigma_{mn})$ arising from domain rotations in respective coordinate direction and always holds the relation $\tilde{\sigma}_{xx} + \tilde{\sigma}_{yy} + \tilde{\sigma}_{zz} = 0$ analogous to magnetostriction. Moreover, for the zero volumetric strain, the relation between effective stresses $\tilde{\sigma}_{kl}$ can also be written as

$$\tilde{\sigma}_{xx}/|\tilde{\sigma}| + \tilde{\sigma}_{yy}/|\tilde{\sigma}| + \tilde{\sigma}_{zz}/|\tilde{\sigma}| = 0 \tag{3.23}$$

where $|\tilde{\sigma}| = \max(|\tilde{\sigma}_{xx}|, |\tilde{\sigma}_{yy}|, |\tilde{\sigma}_{zz}|)$ or $\max(|\tilde{\sigma}_{kl}|)$ and $\tilde{\sigma}_{ij}/|\tilde{\sigma}|$ represents the fraction of magnetostrictive strain in the respective direction with the magnetostrictive strain in the direction of $\tilde{\sigma}$. Ergo, based on the above discussions and neglecting the effect of shear stresses, $\lambda_{0ij}(\sigma_{mn})$ can be approximate as

$$\lambda_{0ij}(\sigma_{mn}) = \begin{cases} \lambda_s \delta_{ij} \left(\frac{\tilde{\sigma}_{ij}}{|\tilde{\sigma}|}\right) \tanh\left(\frac{|\tilde{\sigma}|}{\sigma_s}\right) & \tilde{\sigma} \geq 0 \\ \frac{\lambda_s \delta_{ij}}{2} \left(\frac{\tilde{\sigma}_{ij}}{|\tilde{\sigma}|}\right) \tanh\left(\frac{2|\tilde{\sigma}|}{\sigma_s}\right) & \tilde{\sigma} < 0 \end{cases} \tag{3.24}$$

Hence, $\lambda_{0ij}(\sigma_{mn})\sigma_{ij}$ can be expressed as

$$\lambda_{0ij}(\sigma_{mn})\sigma_{ij} = \begin{cases} \lambda_s \delta_{ij}\sigma_{ij}\left(\frac{\tilde{\sigma}_{ij}}{|\tilde{\sigma}|}\right) tanh\left(\frac{|\tilde{\sigma}|}{\sigma_s}\right) & \tilde{\sigma} \geq 0 \\ \frac{\lambda_s \delta_{ij}\sigma_{ij}}{2}\left(\frac{\tilde{\sigma}_{ij}}{|\tilde{\sigma}|}\right) tanh\left(\frac{2|\tilde{\sigma}|}{\sigma_s}\right) & \tilde{\sigma} < 0 \end{cases} \tag{3.25}$$

Among the various kinds of functions to replicate the magnetization curve, the Langevin function is found to be most appropriate with sound physical and experimental background[50,106]. The response of the free magnetization curve can be represented as a vectorial version of Langevin function[107] ($f(\boldsymbol{a}) = [\coth(|\boldsymbol{a}|) - 1/|\boldsymbol{a}|\,](\boldsymbol{a}/|\boldsymbol{a}|)$) with an isotropic relaxation factor k as follows

$$\boldsymbol{M} = M_x i + M_y j + M_z k = M_s(T) f(k\boldsymbol{H}) \tag{3.26}$$

For instance, M_x can be written as

$$M_x = M_s(T)\left[coth(k|\boldsymbol{H}|) - \frac{1}{k|\boldsymbol{H}|}\right]\frac{H_x}{|\boldsymbol{H}|} \tag{3.27}$$

where $k = 3\chi_m/M_s(T)$ is the relaxation factor, χ_m is initial susceptibility and $|\boldsymbol{H}| = \sqrt{H_k H_k}$ is the magnitude of the magnetic field vector.

Hence, the nonlinear isotropic vector function $f_k^{-1}(M_l)$ can be expressed as,

$$f_k^{-1}(M_l) = \frac{1}{k} f^{-1}\left(\frac{M_l}{M_s(T)}\right)\delta_{kl} \tag{3.28}$$

3.4. Simplified Hysteretic Constitutive Model

In practical applications, when Giant Magnetostrictive materials are used as pre-stressed rods, thin films or beams subjected to an applied magnetic field; the magneto-thermo-elastic coupling effect induces magnetization and output magnetostriction. Thus, for an isotropic magnetostrictive material, employing Eqs. (3.18), (3.20)-(3.21), (3.24)-(3.25)and (3.28), Eqs. (3.15) and (3.16) can be simplified to present a general nonlinear constitutive model in a 3-D case as follows,

$$\varepsilon_{ij} = \frac{1}{E_{in}}\left[(1+\nu)\sigma_{ij} - \nu\sigma_{kk}\delta_{ij}\right] + \frac{\lambda_s}{\left(M_s(T)\right)^2}\left[\frac{3}{2}M_iM_j - \frac{1}{2}M_kM_k\delta_{ij}\right] \tag{3.29}$$

$$+\alpha\delta_{ij}\Delta T + \frac{\beta\delta_{ij}}{(M_s(T))^2}\Delta T M_k M_l$$

$$+\left[1 - \frac{1}{(M_s(T))^2}M_kM_k\right]\begin{cases}\lambda_s\delta_{ij}\left(\frac{\tilde{\sigma}_{ij}}{|\tilde{\sigma}|}\right)tanh\left(\frac{|\tilde{\sigma}|}{\sigma_s}\right) & \tilde{\sigma} \geq 0\\ \frac{\lambda_s\delta_{ij}}{2}\left(\frac{\tilde{\sigma}_{ij}}{|\tilde{\sigma}|}\right)tanh\left(\frac{2|\tilde{\sigma}|}{\sigma_s}\right) & \tilde{\sigma} < 0\end{cases}$$

$$H_k = \frac{1}{k}f^{-1}\left(\frac{M_l}{M_s(T)}\right)\delta_{kl} + N_{kl}M_l - \left(\eta' + \frac{2\beta\delta_{ij}\sigma_{ij}\Delta T}{\mu_o\left(M_s(T)\right)^2}\right)M_l\delta_{kl} - \tag{3.30}$$

$$\frac{\lambda_s M_l}{\mu_o(M_s(T))^2}\left[2\tilde{\sigma}_{kl} - \delta_{kl}\begin{cases}\delta_{ij}\sigma_{ij}\left(\frac{\tilde{\sigma}_{ij}}{|\tilde{\sigma}|}\right)tanh\left(\frac{|\tilde{\sigma}|}{\sigma_s}\right) & \tilde{\sigma} \geq 0\\ \frac{\delta_{ij}\sigma_{ij}}{2}\left(\frac{\tilde{\sigma}_{ij}}{|\tilde{\sigma}|}\right)tanh\left(\frac{2|\tilde{\sigma}|}{\sigma_s}\right) & \tilde{\sigma} < 0\end{cases}\right]$$

The model expressed by Eqs. (3.29) and (3.30) is suitable for both compressive and tensile stress conditions as well as for positive and negative magnetostriction. The above described constitutive model requires following material constants, i.e., the saturation magnetization M_s and the saturation magnetostrictive coefficient λ_s at a reference temperature, saturation stress of magnetic domain rotation σ_s, intrinsic Young's modulus of the material at saturation E_{in}, material's Poisson's ratio ν, Weiss molecular field coefficient η', linear variation coefficient β, inner demagnetizing factor N_{inner}, shape demagnetizing factor N_{shape}, amplification coefficient γ and relaxation factor k. In addition to that, the isotropic parameters λ_s, M_s, β, η', γ and E can be readily determined from physical and mechanical experiments. The amplification coefficient γ can be obtained by determining the slope of the experimental curve for saturation magnetization versus increment

temperature [112]. Increment or decrement in the inner demagnetizing factor depends upon the volume fraction of the material defects such as voids, impurities, cracks etc.[59]. Moreover, the shape demagnetizing factor can be calculated from the approximate expression given in the existing study [60] and this is found to be larger along the short axis up to unity and smaller along the long axis [56]. The Relaxation factor k can be calculated by initial susceptibility and saturation magnetization. The saturation stress of magnetic domain rotation σ_s can be located on material's stress strain curve as intersection of the slope of initial segment and slope of saturation segment [39].

Since $\delta_{ij}\sigma_{ij}\tilde{\sigma}_{ij} = \sigma_{ii}\tilde{\sigma}_{ii} = \frac{3}{2}s_{ij}s_{ji} = \frac{3}{2}tr(\boldsymbol{s}^2) = 3J_2$, where J_2 is the second invariant of the stress deviator tensor $s_{ij} = \sigma_{ij} - \frac{1}{3}\sigma_{ij}\delta_{ij}$; then Eq. (3.30) can be written as

$$H_k = \frac{1}{k}f^{-1}\left(\frac{M_l}{M_s}\right)\delta_{kl} + N_{kl}M_l - \left(\eta' + \frac{2\beta\delta_{ij}\sigma_{ij}\Delta T}{\mu_o\left(M_s(T)\right)^2}\right)M_l\delta_{kl} \tag{3.31}$$

$$-\frac{\lambda_s M_l}{\mu_o {M_s}^2}\left[2\tilde{\sigma}_{kl} - \delta_{kl}\begin{cases}\frac{3J_2}{|\tilde{\sigma}|}tanh\left(\frac{|\tilde{\sigma}|}{\sigma_s}\right) & \tilde{\sigma} \geq 0\\ \frac{3J_2}{2|\tilde{\sigma}|}tanh\left(\frac{2|\tilde{\sigma}|}{\sigma_s}\right) & \tilde{\sigma} < 0\end{cases}\right]$$

Further Eq. (3.31) can be rearranged as

$$\frac{1}{k}f^{-1}\left(\frac{M_l}{M_s(T)}\right)\delta_{kl} = \left(H_{eff}\right)_k \tag{3.32}$$

$$\left(H_{eff}\right)_k = H_k + \eta_{kl}\,M_l \tag{3.33}$$

where H_{eff} is the effective magnetic field and η_{kl} is a second rank symmetric tensor; thus, we can get

$$\eta_{kl} = \left(\eta' + \frac{2\beta\delta_{ij}\sigma_{ij}\Delta T}{\mu_o\left(M_s(T)\right)^2}\right)\delta_{kl} - N_{kl}$$

$$+\frac{\lambda_s}{\mu_o(M_s(T))^2}\left[2\tilde{\sigma}_{kl} - \delta_{kl}\begin{cases}\frac{3J_2}{|\tilde{\sigma}|}tanh\left(\frac{|\tilde{\sigma}|}{\sigma_s}\right) & \tilde{\sigma} \geq 0\\ \frac{3J_2}{2|\tilde{\sigma}|}tanh\left(\frac{2|\tilde{\sigma}|}{\sigma_s}\right) & \tilde{\sigma} < 0\end{cases}\right]$$

As discussed earlier, the nonlinear isotropic vector function $f_k^{-1}(M_l)$ can be expressed in the form of inverse vectorial Langevin function. An assumption is made here that the domain wall motion is not considered, and this is consistent with derivation of Eqs. (3.29) and (3.30) as we are considering only reversible changes along the thermodynamic (anhysteretic) path. Thus, Eq. (3.32) can be rewritten as

$$(M_{an})_i = M_s(T)\left[coth\left(k\sqrt{\left(H_{eff}\right)_k\left(H_{eff}\right)_k}\right) - \frac{1}{k\sqrt{\left(H_{eff}\right)_k\left(H_{eff}\right)_k}}\right]\frac{\left(H_{eff}\right)_i}{\sqrt{\left(H_{eff}\right)_k\left(H_{eff}\right)_k}} \tag{3.34}$$

or can be concisely expressed in vector form as

$$\boldsymbol{M_{an}} = M_s(T)\left[\coth\left(k\left|\boldsymbol{H_{eff}}\right|\right) - \frac{1}{k\left|\boldsymbol{H_{eff}}\right|}\right]\frac{\boldsymbol{H_{eff}}}{\left|\boldsymbol{H_{eff}}\right|}$$

where $\left|\boldsymbol{H_{eff}}\right| = \sqrt{\left(H_{eff}\right)_k\left(H_{eff}\right)_k}$ is the magnitude of the effective magnetic field vector.

Further, it is considered that the domain wall motions under the applied magnetic field are however impeded by the presence of pinning sites in the material such as nonmagnetic inclusions, voids, or regions of inhomogeneous stresses. Jiles et al.[46] considered the nature of these imperfections collectively as pinning sites. Therefore, these pinning sites present a

restraining force which inhibits changes in magnetization. Thus, the total magnetization $\boldsymbol{M}$ may be split into two terms, as irreversible changes in magnetization $\boldsymbol{M_{irr}}$ due to the energy dissipated against the pinning sites and reversible changes $\boldsymbol{M_{rev}}$ that occur in ideal or unpinned specimen in which the energy increases with change in magnetization. Hence, the total magnetization $\boldsymbol{M}$ can be expressed as,

$$\boldsymbol{M} = \boldsymbol{M_{rev}} + \boldsymbol{M_{irr}} \tag{3.35}$$

and the magnetic induction $\boldsymbol{B}$ is introduced by

$$\boldsymbol{B} = \mu_o(\boldsymbol{H} + \boldsymbol{M}) \tag{3.36}$$

As stated in [46], the pinning sites hindered the magnetization from striving towards anhysteretic value, thus the scalar value $(1/\delta K)(\, M_{an} - \, M_{irr})$ is interpreted as the force impelling the domain wall motion. Here, the parameter K (scalar) is pinning constant related to hysteresis loss and the parameter δ take the value $+1$ when H increases and -1 when H decreases for ensuring that the pinning opposes changes in magnetization. Bregqvist [105], in a generalized vector case, introduced a similar auxiliary vector variable $\boldsymbol{\chi'} = \overleftrightarrow{K}^{-1}(\, \boldsymbol{M_{an}} - \boldsymbol{M_{irr}})$ with the pinning parameter represented by $\overleftrightarrow{K}$, which is a second rank symmetric tensor; possess identical diagonal terms in isotropic case. The changes in $\boldsymbol{M_{irr}}$ parallel to $\boldsymbol{\chi'}$, can be expressed as [105]

$$d\boldsymbol{M_{irr}} = \boldsymbol{\chi'}.|\boldsymbol{\chi'}|^{-1}[\boldsymbol{\chi'}.d\boldsymbol{H_{eff}}]^{+} \tag{3.37}$$

where, $[\boldsymbol{\chi'}.d\boldsymbol{H_{eff}}]^{+} = \boldsymbol{\chi'}.d\boldsymbol{H_{eff}}$ if $\boldsymbol{\chi'}.d\boldsymbol{H_{eff}} > 0$, and $[\boldsymbol{\chi'}.d\boldsymbol{H_{eff}}]^{+} = 0$ if $\boldsymbol{\chi'}.d\boldsymbol{H_{eff}} \leq 0$.

The vector version of reversible magnetization component $d\boldsymbol{M_{rev}}$ is given as

$$d\boldsymbol{M_{rev}} = \overleftrightarrow{c}.[d\boldsymbol{M_{an}} - \, d\boldsymbol{M_{irr}}] \tag{3.38}$$

Here, $\overleftrightarrow{c}$ is also a second rank symmetric tensor of reversible coefficients.

The total differential magnetization can be obtained by rearranging Eqs. (3.35)-(3.38) as [105]

$$d\boldsymbol{M} = \boldsymbol{\chi}.|\boldsymbol{\chi}|^{-1}[\boldsymbol{\chi}.d\boldsymbol{H_{eff}}]^{+} + \overleftrightarrow{c}.d\boldsymbol{M_{an}} \tag{3.39}$$

The new vector variable nomenclature is noted as

$$\boldsymbol{\chi} = \overleftrightarrow{K}^{-1}(\boldsymbol{M_{an}} - \boldsymbol{M}) \tag{3.40}$$

From Eq. (35), change in magnetization $d\boldsymbol{M}$ with hysteresis loss can be evaluated for any variation of applied magnetic field $\boldsymbol{H}$.

Leite et. al.[107] revised the expression of total differential magnetization (Eq. (3.39)) related to the magnetic field for better numerical behaviour as

$$d\boldsymbol{M} = \begin{cases} [\boldsymbol{\chi}.|\boldsymbol{\chi}|^{-1}.\boldsymbol{\chi} + \overleftrightarrow{c}.\overleftrightarrow{\xi}].d\boldsymbol{H_{eff}} & \boldsymbol{\chi}.d\boldsymbol{H_{eff}} > 0 \\ \overleftrightarrow{c}.\overleftrightarrow{\xi}.d\boldsymbol{H_{eff}} & \boldsymbol{\chi}.d\boldsymbol{H_{eff}} \leq 0 \end{cases} \quad if \tag{3.41}$$

Let us observe the tensor $\overleftrightarrow{\xi}$ that shows the variation of anhysteretic magnetization $d\boldsymbol{M_{an}}$ as a function of effective field $\boldsymbol{H_{eff}}$. For 3-D modelling in Cartesian coordinate system $O-x,y,z$, $\overleftrightarrow{\xi}$ is given as

$$\overleftrightarrow{\xi} = \begin{bmatrix} \frac{dM_{anx}}{dH_{effx}} & 0 & 0 \\ 0 & \frac{dM_{any}}{dH_{effy}} & 0 \\ 0 & 0 & \frac{dM_{anz}}{dH_{effz}} \end{bmatrix} \tag{3.42}$$

With the help of Eq. (3.34), x component of anhysteretic magnetization M_{anx} can be written as

$$M_{anx} = M_s(T)\left[coth\left(k\left|\boldsymbol{H_{eff}}\right|\right) - \frac{1}{k\left|\boldsymbol{H_{eff}}\right|}\right]\frac{H_{effx}}{\left|\boldsymbol{H_{eff}}\right|} \tag{3.43}$$

Then the derivative of M_{anx} with respect to H_{effx} is derived below

$$\frac{dM_{anx}}{dH_{effx}} = kM_s(T)\left[1 - coth^2\left(k\left|\boldsymbol{H_{eff}}\right|\right) + \frac{1}{\left(k\left|\boldsymbol{H_{eff}}\right|\right)^2}\right]\frac{H_{effx}^2}{\left|\boldsymbol{H_{eff}}\right|^2} \tag{3.44}$$

$$+ M_s(T)\left[coth\left(k\left|\boldsymbol{H_{eff}}\right|\right) - \frac{1}{k\left|\boldsymbol{H_{eff}}\right|}\right]\left[\frac{1}{\left|\boldsymbol{H_{eff}}\right|} - \frac{H_{effx}^2}{\left|\boldsymbol{H_{eff}}\right|^3}\right]$$

Another observation is that M_{anx} and so also $\frac{dM_{anx}}{dH_{ex}}$ become singular if the argument of $coth$ function is very small. In this case, M_{anx} can be expanded in a Taylor series and thereby retaining its first two terms we obtain

$$M_{anx} = M_s(T)\frac{kH_{effx}}{3} \quad \text{and} \tag{3.45}$$

$$\frac{dM_{anx}}{dH_{effx}} = \frac{kM_s(T)}{3} \tag{3.46}$$

In the subsequent sections, the applicability of the model for the Terfenol-D rod for two-dimensional and one-dimensional problems has been discussed.

3.4.1. 2-D model for magnetostrictive thin films and plates

Giant magnetostrictive material (GMM) amorphous films and plates exhibit excellent low fields and soft magnetic properties. Two dimensional models are required for describing their magneto-thermo-elastic coupling behavior. Therefore, a 2-D coupled constitutive model with potential application in in plates/films has been derived by considering plane stress condition (i.e. $\sigma_z = \tau_{zx} = \tau_{zy} = 0$) with the magnetic field applied parallel $(H_z = 0)$ or perpendicular $\left(H_x = H_y = 0\right)$ to the plane. Now. The expressions for $\tilde{\sigma}_{kl}$, λ_{0ij} and $\lambda_{0ij}\sigma_{ij}$ are given as

$$\tilde{\sigma}_{xx} = \sigma_x - \frac{1}{2}\sigma_y, \qquad \tilde{\sigma}_{yy} = \sigma_y - \frac{1}{2}\sigma_x, \tag{3.47}$$

$$\tilde{\sigma}_{zz} = -\frac{1}{2}(\sigma_x + \sigma_y), \quad \tilde{\tau}_{xy} = \frac{3}{2}\tau_{xy}, \quad \tilde{\tau}_{zx} = \tilde{\tau}_{zy} = 0$$

$$\lambda_{0x} = \begin{cases} \lambda_s\left(\frac{\tilde{\sigma}_{xx}}{|\tilde{\sigma}|}\right) tanh\left(\frac{|\tilde{\sigma}|}{\sigma_s}\right) & \tilde{\sigma} \geq 0 \\ \frac{\lambda_s}{2}\left(\frac{\tilde{\sigma}_{xx}}{|\tilde{\sigma}|}\right) tanh\left(\frac{2|\tilde{\sigma}|}{\sigma_s}\right) & \tilde{\sigma} < 0 \end{cases} \tag{3.48}$$

$$\lambda_{0y} = \begin{cases} \lambda_s\left(\frac{\tilde{\sigma}_{yy}}{|\tilde{\sigma}|}\right) tanh\left(\frac{|\tilde{\sigma}|}{\sigma_s}\right) & \tilde{\sigma} \geq 0 \\ \frac{\lambda_s}{2}\left(\frac{\tilde{\sigma}_{yy}}{|\tilde{\sigma}|}\right) tanh\left(\frac{2|\tilde{\sigma}|}{\sigma_s}\right) & \tilde{\sigma} < 0 \end{cases} \tag{3.49}$$

$$\lambda_{0ij}\sigma_{ij} = \lambda_s \begin{cases} \frac{3J_2}{|\tilde{\sigma}|} tanh\left(\frac{|\tilde{\sigma}|}{\sigma_s}\right) & \tilde{\sigma} \geq 0 \\ \frac{3J_2}{2|\tilde{\sigma}|} tanh\left(\frac{2|\tilde{\sigma}|}{\sigma_s}\right) & \tilde{\sigma} < 0 \end{cases} \tag{3.50}$$

Thus, for an isotropic magnetostrictive material, the 2-D formulations can be deduced from Eqs. (3.29) and (3.30) in the matrix forms as follows.

3.4.1.1. For magnetic field parallel to film/plate

$$\begin{Bmatrix} \varepsilon_x \\ \varepsilon_y \\ \gamma_{xy} \end{Bmatrix} = \begin{bmatrix} \frac{1}{E_{in}} & -\frac{\nu}{E_{in}} & 0 \\ -\frac{\nu}{E_{in}} & \frac{1}{E_{in}} & 0 \\ 0 & 0 & \frac{1}{G} \end{bmatrix} \begin{Bmatrix} \sigma_x \\ \sigma_y \\ \tau_{xy} \end{Bmatrix} + \begin{Bmatrix} \lambda_{0x} + \alpha\Delta T \\ \lambda_{0y} + \alpha\Delta T \\ 0 \end{Bmatrix} +$$

$$\frac{1}{\left(M_s(T)\right)^2} \begin{bmatrix} \lambda_s - \lambda_{0x} + \beta\Delta T & -\frac{\lambda_s}{2} - \lambda_{0x} + \beta\Delta T & 0 \\ -\frac{\lambda_s}{2} - \lambda_{0y} + \beta\Delta T & \lambda_s - \lambda_{0y} + \beta\Delta T & 0 \\ 0 & 0 & 3 \end{bmatrix} \times \begin{Bmatrix} M_x^2 \\ M_y^2 \\ M_x M_y \end{Bmatrix} \tag{3.51}$$

$$\begin{Bmatrix} H_x \\ H_y \end{Bmatrix} = \frac{1}{k}\begin{bmatrix} f^{-1}\left(\frac{M_x}{M_s(T)}\right) & 0 \\ 0 & f^{-1}\left(\frac{M_y}{M_s(T)}\right) \end{bmatrix} \tag{3.52}$$

$$+\left(\begin{bmatrix} N_{xx} & 0 \\ 0 & N_{yy} \end{bmatrix} - \left\{\eta' + \frac{2\beta I_\sigma \Delta T}{\mu_o\left(M_s(T)\right)^2}\right\}\begin{bmatrix} 1 & 0 \\ 0 & 1 \end{bmatrix}\right)\begin{Bmatrix} M_x \\ M_y \end{Bmatrix}$$

$$-\left(\frac{\lambda_s}{\mu_o\left(M_s(T)\right)^2}\begin{bmatrix} 2\tilde{\sigma}_x - \lambda_{0ij}\sigma_{ij} & 2\tilde{\tau}_{xy} \\ 2\tilde{\tau}_{xy} & 2\tilde{\sigma}_y - \lambda_{0ij}\sigma_{ij} \end{bmatrix}\right)\begin{Bmatrix} M_x \\ M_y \end{Bmatrix}$$

Here, $\gamma_{xy} = 2\varepsilon_{xy}$ is engineering shear strain and I_σ is the first invariant of stress.

3.4.1.2. For magnetic field perpendicular to film/plate

$$\begin{Bmatrix} \varepsilon_x \\ \varepsilon_y \\ \gamma_{xy} \end{Bmatrix} = \begin{bmatrix} \frac{1}{E_{in}} & -\frac{\nu}{E_{in}} & 0 \\ -\frac{\nu}{E_{in}} & \frac{1}{E_{in}} & 0 \\ 0 & 0 & \frac{1}{G} \end{bmatrix}\begin{Bmatrix} \sigma_x \\ \sigma_y \\ \tau_{xy} \end{Bmatrix} + \begin{Bmatrix} \lambda_{0x} + \alpha\Delta T \\ \lambda_{0y} + \alpha\Delta T \\ 0 \end{Bmatrix} \tag{3.53}$$

$$+\frac{M_z^2}{\left(M_s(T)\right)^2}\begin{Bmatrix} -\frac{\lambda_s}{2} - \lambda_{0x} + \beta\Delta T \\ -\frac{\lambda_s}{2} - \lambda_{0y} + \beta\Delta T \\ 0 \end{Bmatrix}$$

$$H_z = \frac{1}{k}f^{-1}\left(\frac{M_z}{M_s(T)}\right) - \left(\eta' - N_{zz} + \frac{2\beta I_\sigma \Delta T}{\mu_o\left(M_s(T)\right)^2}\right)M_z \tag{3.54}$$

$$-\frac{\lambda_s}{\mu_o\left(M_s(T)\right)^2}\left[2\tilde{\sigma}_z - \lambda_{0ij}\sigma_{ij}\right]M_z$$

Magnetostrictive films are usually deposited on substrate or sheets by DC sputtering technique, and they possess the ubiquitous out-of-plane preferred spin orientation. Upon cooling, owing to different thermal expansion coefficients of the film and the substrate/sheets, residual biaxial stresses ($\sigma_x = \sigma_y = \sigma$) are developed. Then

$$\tilde{\sigma}_{xx} = \sigma/2, \qquad \tilde{\sigma}_{yy} = \sigma/2, \qquad \tilde{\sigma} = \tilde{\sigma}_{zz} = -\sigma,$$

$$\tilde{\tau}_{xy} = \tilde{\tau}_{zx} = \tilde{\tau}_{zy} = 0$$

Thus Eqs. (3.51), (3.52), (3.53) and (3.54) can be rewritten as

3.4.1.3. For magnetic field parallel to film (Along the *x*-direction)

$$\varepsilon_x = \frac{1-\nu}{E_{in}}\sigma + \alpha\Delta T + \frac{\beta\Delta T M_x^2}{\left(M_s(T)\right)^2} + \begin{cases} \frac{\lambda_s}{2}tanh\left(\frac{\sigma}{\sigma_s}\right) + \left[2 - tanh\left(\frac{\sigma}{\sigma_s}\right)\right]\frac{\lambda_s}{2\left(M_s(T)\right)^2}M_x^2 & \sigma \le 0 \\ \frac{\lambda_s}{4}tanh\left(\frac{2\sigma}{\sigma_s}\right) + \left[4 - tanh\left(\frac{2\sigma}{\sigma_s}\right)\right]\frac{\lambda_s}{4\left(M_s(T)\right)^2}M_x^2 & \sigma > 0 \end{cases} \tag{3.55}$$

$$\varepsilon_y = \frac{1-\nu}{E_{in}}\sigma + \alpha\Delta T + \frac{\beta\Delta T M_x^2}{\left(M_s(T)\right)^2} + \begin{cases} \frac{\lambda_s}{2}tanh\left(\frac{\sigma}{\sigma_s}\right) - \left[1 + tanh\left(\frac{\sigma}{\sigma_s}\right)\right]\frac{\lambda_s}{2\left(M_s(T)\right)^2}M_x^2 & \sigma \le 0 \\ \frac{\lambda_s}{4}tanh\left(\frac{2\sigma}{\sigma_s}\right) - \left[2 + tanh\left(\frac{2\sigma}{\sigma_s}\right)\right]\frac{\lambda_s}{4\left(M_s(T)\right)^2}M_x^2 & \sigma > 0 \end{cases} \tag{3.56}$$

$$\gamma_{xy} = 0 \tag{3.57}$$

$$H_x = \frac{1}{k}f^{-1}\left(\frac{M_x}{M_s(T)}\right) - \left(\eta' - N_{xx} + \frac{4\beta\sigma\Delta T}{\mu_o\left(M_s(T)\right)^2}\right)M_x - \frac{\lambda_s\sigma}{\mu_o\left(M_s(T)\right)^2}M_x \begin{cases} 1 - tanh\left(\frac{\sigma}{\sigma_s}\right) & \sigma \le 0 \\ 1 - \frac{1}{2}tanh\left(\frac{2\sigma}{\sigma_s}\right) & \sigma > 0 \end{cases} \tag{3.58}$$

$$H_x = \frac{1}{k} f^{-1}\left(\frac{M_x}{M_s(T)}\right) - \left(\eta' - N_{xx} + \frac{4\beta\sigma\Delta T}{\mu_o\left(M_s(T)\right)^2}\right) M_x \tag{3.59}$$

$$- \frac{\lambda_s \sigma}{\mu_o\left(M_s(T)\right)^2} M_x \begin{cases} 1 - tanh\left(\frac{\sigma}{\sigma_s}\right) & \sigma \leq 0 \\ 1 - \frac{1}{2} tanh\left(\frac{2\sigma}{\sigma_s}\right) & \sigma > 0 \end{cases}$$

$$H_y = 0 \tag{3.60}$$

3.4.1.4. For magnetic field perpendicular to film (Along the z-direction)

$$\varepsilon_x = \varepsilon_y = \frac{1-\nu}{E_{in}}\sigma + \alpha\Delta T + \frac{\beta\Delta T M_z^2}{\left(M_s(T)\right)^2} \tag{3.61}$$

$$+ \begin{cases} \frac{\lambda_s}{2}\tanh\left(\frac{\sigma}{\sigma_s}\right) - \left[1 + \tanh\left(\frac{\sigma}{\sigma_s}\right)\right]\frac{\lambda_s}{2\left(M_s(T)\right)^2} M_z^2 & \sigma \leq 0 \\ \frac{\lambda_s}{4}\tanh\left(\frac{2\sigma}{\sigma_s}\right) - \left[2 + \tanh\left(\frac{2\sigma}{\sigma_s}\right)\right]\frac{\lambda_s}{4\left(M_s(T)\right)^2} M_z^2 & \sigma > 0 \end{cases}$$

$$\gamma_{xy} = 0 \tag{3.62}$$

$$H_z = \frac{1}{k} f^{-1}\left(\frac{M_z}{M_s(T)}\right) - \left(\eta' - N_{zz} + \frac{4\beta\sigma\Delta T}{\mu_o\left(M_s(T)\right)^2}\right) M_Z \tag{3.63}$$

$$+ \frac{\lambda_s \sigma}{\mu_o\left(M_s(T)\right)^2} M_z \begin{cases} 2 + tanh\left(\frac{\sigma}{\sigma_s}\right) & \sigma \leq 0 \\ 2 + \frac{1}{2} tanh\left(\frac{2\sigma}{\sigma_s}\right) & \sigma > 0 \end{cases}$$

3.4.2. 1-D model for magnetostrictive rods

As a primary element of the actuator, Terfenol D rods are often subjected to axial pre-stress and axial applied magnetic field. The constitutive relations among the stress, strain, magnetic field, and magnetization along the rod axis are deduced as

$$\varepsilon = \frac{\sigma}{E_{in}} + \alpha\Delta T + \frac{\beta\Delta T M^2}{\left(M_s(T)\right)^2} + \begin{cases} \lambda_s \tanh\left(\frac{\sigma}{\sigma_s}\right) + \left[1 - \tanh\left(\frac{\sigma}{\sigma_s}\right)\right]\frac{\lambda_s}{\left(M_s(T)\right)^2}M^2 & \sigma \geq 0 \\ \frac{\lambda_s}{2}\tanh\left(\frac{2\sigma}{\sigma_s}\right) + \left[2 - \tanh\left(\frac{2\sigma}{\sigma_s}\right)\right]\frac{\lambda_s}{2\left(M_s(T)\right)^2}M^2 & \sigma < 0 \end{cases} \tag{3.64}$$

$$H = \frac{1}{k} f^{-1}\left(\frac{M}{M_s(T)}\right) - \left(\eta' - N + \frac{2\beta\sigma\Delta T}{\mu_o\left(M_s(T)\right)^2}\right)M - \frac{\lambda_s\sigma}{\mu_o\left(M_s(T)\right)^2}M \begin{cases} 2 - \tanh\left(\frac{\sigma}{\sigma_s}\right) & \sigma \geq 0 \\ 2 - \frac{1}{2}\tanh\left(\frac{2\sigma}{\sigma_s}\right) & \sigma < 0 \end{cases} \tag{3.65}$$

3.4.3. Solution Algorithm

Major hysteresis loops can be obtained by varying the H field amplitudes progressively in a cycle starting from the demagnetized state. These loops are widely used to describe the magnetic properties and general shape of magnetostrictive materials. A solution procedure for the calculation of the magnetization **M** with respect to **H** in the major hysteresis loops is summarized in **Figure 3.2**. Material parameters are requisite entry data that are optimized from physical and experimental observations. The magnetic field equations [such as Eqs. (3.30)] can be rewritten similar to Eqs. (3.32) and (3.33). The anhysteretic magnetization $\mathbf{M_{an}}$ can be evaluated iteratively using Eq. (3.34) for the trial values of effective field $\boldsymbol{H_{eff}}$. The iteration can be initialized under the assumption of $\boldsymbol{H_{eff}} = \mathbf{H}$. The updated effective field $\boldsymbol{H_{eff}}$ is determined from Eq. (3.32) using previously evaluated $\mathbf{M}_{an}^{prev}$ and further, using the updated $\boldsymbol{H_{eff}}$, a new revised value of $\mathbf{M_{an}}$ can be obtained. This iteration is continued until the convergence criterion is met (i.e. $\left|\mathbf{M_{an}} - \mathbf{M}_{an}^{prev}\right| / \left|\mathbf{M}_{an}^{prev}\right| < 0.001$). The Euler's

method is employed to compute the total hysteretic magnetization by Eq. (3.41) using with the help of acquired values of $\mathbf{M_{an}}$ and $\boldsymbol{H_{eff}}$. Lastly, the hysteretic magnetic induction $\boldsymbol{B}$ and the nonlinear hysteretic magnetostriction can be determined from Eq. (3.36) and Eq. (3.29), respectively, under the combined effect of the applied magnetic field, prestresses and temperature.

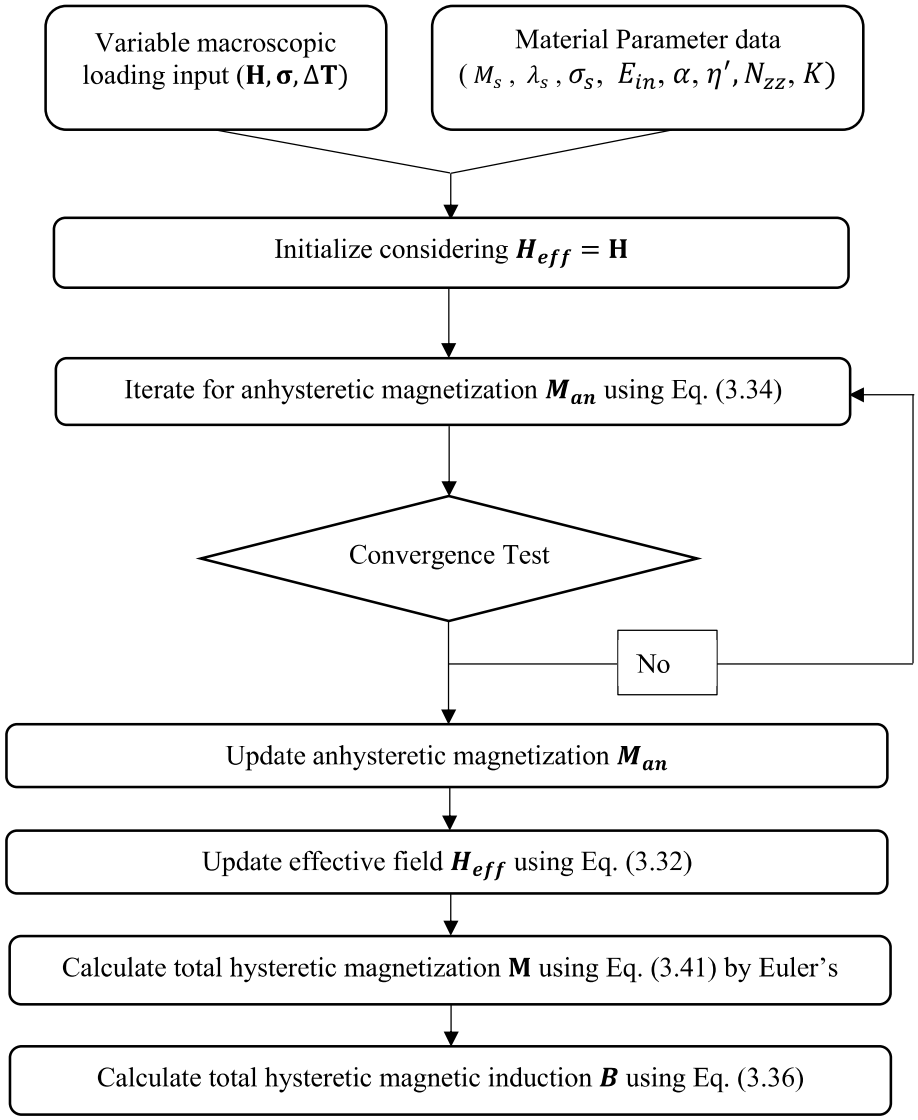

Figure 3.2 A solution algorithm for the generalized coupled nonlinear hysteretic constitutive model for major hysteresis loops

However, the above discussed algorithm for 3-D hysteresis can accommodate small hysteresis loops and inner symmetric loops with some discrepancies but lead to predicting

errors for the high order reversals [115–117]. This may be seen as a limitation of this algorithm which is not completely complemented to such processes.

3.5. Simulation Physics

In this section, a computational framework is suggested to evaluate the response of the magnetostrictive devices that are governed by the coupled magneto-thermo-elastic physical domains. Continuum mechanics of magneto-elastic solids in the thermal environment can be presented with Maxwell equations, conservation of linear momentum and transient heat conduction equation in strong form. This coupled physics problem can be simulated with a finite element based COMSOL Multiphysics v5.0 using the Magnetic Field, Solid Mechanics, and Heat Transfer modules. As a basis for a transient solver, the relations defined by Maxwell equations, linear momentum balance equation and heat conduction equation were employed.

In low-frequency devices, the effects corresponding to the change of electrical energy density can be neglected with respect to the change of the magnetic energy density and the loss density; the Amperes law can be yielded as $\nabla \times \boldsymbol{H} = \boldsymbol{J}$ where $\boldsymbol{J}$ is the current density. Since the magnetic flux density shall have zero divergence, thus it can be expressed as $\boldsymbol{B} = \nabla \times \boldsymbol{A}$, where $\boldsymbol{A}$ signifies a vector magnetic potential. The Faraday-Lenz law for conducting materials relates the electric field $\boldsymbol{E}$ to the vector magnetic potential and to the scalar electric potential φ as $\boldsymbol{E} = -\frac{\partial \boldsymbol{A}}{\partial t} - \nabla\varphi$. The relationship between $\boldsymbol{J}$ and $\boldsymbol{E}$ for a metallic conductor specified by the conductivity σ_E, i.e., $\boldsymbol{J} = \sigma_E \boldsymbol{E}$. The introduction of the Faraday-Lenz law in the Amperes law provides a strong form equation for magnetic field $\boldsymbol{H}$ as

$$\nabla \times \boldsymbol{H} + \sigma_E \frac{\partial \boldsymbol{A}}{\partial t} = \boldsymbol{J_s} \tag{3.66}$$

where $\boldsymbol{J_s} = -\sigma_E \nabla\varphi$ is source current density and $\sigma_E \frac{\partial \boldsymbol{A}}{\partial t} = \boldsymbol{J_e}$ is the eddy-current term.

The linear momentum balance equation for the elastic field can be written as

$$\nabla . \boldsymbol{\sigma} + \boldsymbol{f_b} = \rho \frac{\partial^2 \boldsymbol{u}}{\partial t^2} \tag{3.67}$$

where $\boldsymbol{u}$ is displacement, $\boldsymbol{\sigma}$ is stress, ρ is density and $\boldsymbol{f_b}$ is body force per unit volume.

The transient heat conduction equation using the temperature T as variable given as

$$\nabla . (k \nabla T) + \boldsymbol{q} = \rho c \frac{\partial T}{\partial t} \tag{3.68}$$

where c is the specific heat of the material, $\boldsymbol{q}$ heat energy generated per unit volume, and k is the thermal conductivity tensor of the material.

3.5.1. Model Definition

In order to validate the proposed constitutive model, two transient models of Terfenol-D actuators based on rods and films were implemented in COMSOL Multiphysics v5.0. The finite element model needed source current density $\boldsymbol{J_s}$ as input and can be evaluated with COMSOL's multi-turn coil feature. Upon specifying the total coil current I_{coil}, the electromagnetic coil applies the source current density in the direction of the wires as

$$J_s = \frac{N_{coil} I_{coil}}{A_{coil}} \tag{3.69}$$

where N_{coil} is the number of turns in the coil and A_{coil} is the total cross-sectional area of the coil domain.

The nonlinear constitutive behaviour of Terfenol-D rod is described using equations (3.29) and (3.30). The inelastic strain contribution of the non-linear stress-strain relationship proposed in equation (3.29) is defined as an external strain with the existing elastic material node. The hysteretic magnetization behaviour of Terfenol-D rod proposed in equation 36 [Eq. (3.30)] is characterized using the general $\boldsymbol{H}(\boldsymbol{B})$ relation in the external material node.

The general $\boldsymbol{H}(\boldsymbol{B})$ relation is coded in the C programming language using the solution algorithm, as shown in **Figure 3.2**. The response of Terfenol-D can be quantified in COMSOL Multiphysics for a different set of initial and boundary conditions.

3.5.1.1. For actuators based on rods

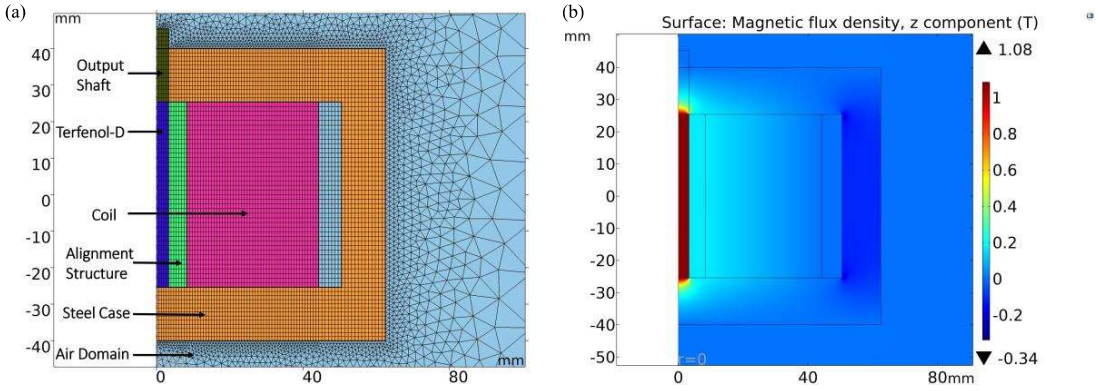

Figure 3.3: 2D axisymmetric geometry of actuator based on Terfenol-D rod with **(a)** mapped meshing of the actuator and **(b)** magnetic flux density distribution along the longitudinal direction of Terfenol-D rod in COMSOL Multiphysics

Actuators based on Terfenol-D rod is being modelled using the 2D axisymmetric space. The actuator has a low carbon steel housing enclosing a Terfenol-D rod, an excitation coil and a piston. The dimensions of the Terfenol-D rod are 6.35 mm in diameter and 50.8 mm in length. The excitation coil has 985 turns. **Figure 3.3 (a)** presents the 2D mapped meshing of the actuator and triangular meshing of the air domain around the whole actuator for high fidelity simulations. **Figure 3.3 (b)** shows the magnetic flux density along the length of the Terfenol-D rod when excitation current is 7 A, and the pre-stress is 20 MPa at room temperature. It is noted that the distribution of magnetic flux density adheres close to the homogenous value of 1 T.

3.5.1.2. For actuators based on films

Actuators based on Terfenol-D thin films is studied with full 3-D transient model. A composite cantilever beam is considered, which has a prestressed Terfenol-D layer ($10\mu m$)

bonded to a compliant Silicon (Si) substrate $(50\mu m)$, a drive coil and a pair of steel yoke. The actuator is excited by applying a current input to coil. The system is surrounded by a large air domain, thus magnetic potential at its outer boundaries is negligible. **Figure 3.4 (a)** shows the mesh geometry used for finite element solution. **Figure 3.4 (b)** displays the distribution of magnetic flux density norm in Terfenol-D layer.

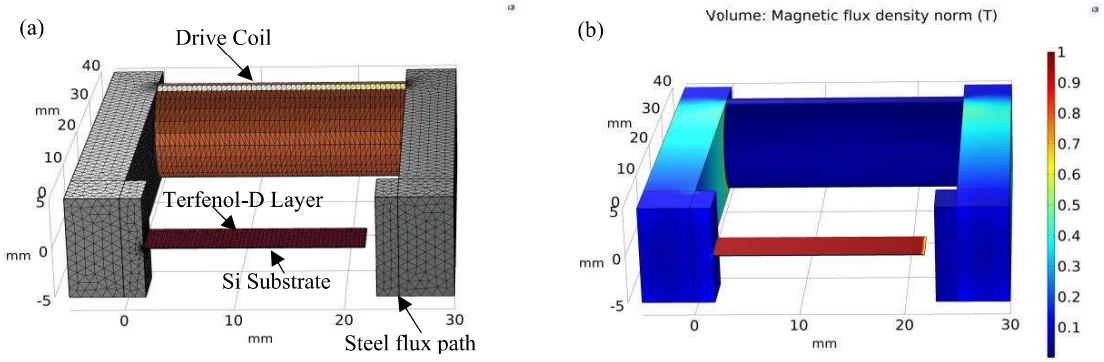

Figure 3.4: 3-D geometry of actuator based on Terfenol-D film with **(a)** meshing of the actuator and **(b)** magnetic flux density norm distribution in COMSOL Multiphysics

3.6. Verification With Experiments And Discussions

Case studies of 1D rods/bars and more importantly for 2D thin films/plates have been conducted and the relative influence of magnetization, elastic and the thermal parameters are characterized. In order to predict the effectiveness of the present coupled nonlinear hysteresis constitutive model, comparative studies are carried out for the present constitutive model predictions with reference to the available experimental observations and the existing theoretical models of magnetostrictive material (such as Terfenol-D) under the combined external stimuli. The magnetization and the magnetostriction curves varying with the applied magnetic field are delineated to assess the combined effect of pre-stress and temperature. The theoretical modelling error for each curve is evaluated by averaging the normalized root mean square error, which can be defined as

$$(E_{nrms})_{avg} = \frac{1}{j}\left[\frac{1}{range(\boldsymbol{X})}\sqrt{\frac{\sum_{i=1}^{N_i}(X_{ij}-Y_{ij})^2}{N_j}}\right] \tag{3.70}$$

where X_{ij} and Y_{ij} are the i^{th} component of j^{th} curve of theoretical modelling predictions and experimental data, respectively, N_j is the points contains by each curve, $range(\boldsymbol{X})$ is the difference between the extreme values of the entire set. The maximum error and average error are measured to quantify the efficient performance of the model. Table 3-1 summarizes the average and maximum error for different experimental data sets.

Table 3-1: Normalized root mean square errors (average and maximum errors) obtained with the coupled nonlinear hysteretic model

Experimental Data	Average error (%)	Maximum error (%)
Moffett et al.[14] (Magnetostriction curves)	1.05	2.3
Clark et al.[13] (Temperature-dependent Magnetization curves)	2.8	5.2
Clark et al.[13] (Temperature-dependent Magnetostriction curves)	2.1	4.3
Kellogg et al.[17] (Stress-Strain curves)	1.6	7.6
Schatz's et al.[16] (magnetization curves for film under tensile stress)	1.26	1.9
Schatz's et al.[16] (magnetization curves for film under compressive stress)	2.3	5.1
Schatz's et al.[16] (magnetostriction parallel to film plane)	2.1	4.6

3.6.1. Case Study 1: For magnetostrictive rods

At first, we validate the response predicted by the proposed constitutive model for magnetostrictive rods along its longitudinal axis. The experimental stress-strain data reported by Kellogg et al.[17] for Terfenol-D are reproduced in **Figure 3.5**, as well as compared with the curves predicted by the present model and the phenomenological 3-D model introduced by Jin et al.[54]. Based on the experimental curves, the material parameters can be optimized as listed in **Table 3-2.**

Table 3-2: Optimized model parameters for different experimental data sets

Property	Kellogg et al.[17] $(Tb_{0.3}Dy_{0.7}Fe_{0.2})$	Moffett et al.[14] $(Tb_{0.3}Dy_{0.7}Fe_{1.93})$	Clark et al.[13] $(Tb_{0.3}Dy_{0.7}Fe_{1.9})$
M_s $(\times 10^5$ A/m)	8.5	6.3	8.2
λ_s (ppm)	1580	1400	1820
σ_s (MPa)	45	150	150
E_{in}(GPa)	110	110	110
η'	0.062	0.042	0.042
T_c (°C)	383.3	383.3	383.3
β $(\times 10^{-6}$ °C$^{-1})$	-5.6	-5.6	-5.6
α $(\times 10^{-6}$ °C$^{-1})$	12	12	12
c	0.2	0.18	0.18
χ_m	19	37	37
K (A/m)	7500	4000	6000
N_{zz}	0	0	0

Since the geometric demagnetization factor approaches zero for a thin rod specimen along its longitudinal axis [56] and considering no internal defects in material, we can set the demagnetizing factor as $N_{zz} = 0$. This comparison shows that the Jin et al.[54] model is

only able to predict the curve efficiently in the region of low stresses. The discrepancies are significant at higher stresses because their model considers the nonlinear part of elastic strain to be linear, deviating from the realistic observations. The pertinent physics of the later exhibiting nonlinear elasticity is included in the present constitutive model. Hence, the predictions are in considerably good agreement (1.2% root mean square error) with the experimental observations. In this work, the nonlinear part of elastic strain for macroscopic bulk materials is estimated by a vector function of the hyperbolic tangent, i.e. based on the knowledge of isotropic elasticity theory and the physical facts of magnetostrictive volumetric strain [4] and hence able to address the saturation phenomenon of nonlinear part of elastic strain at high stresses.

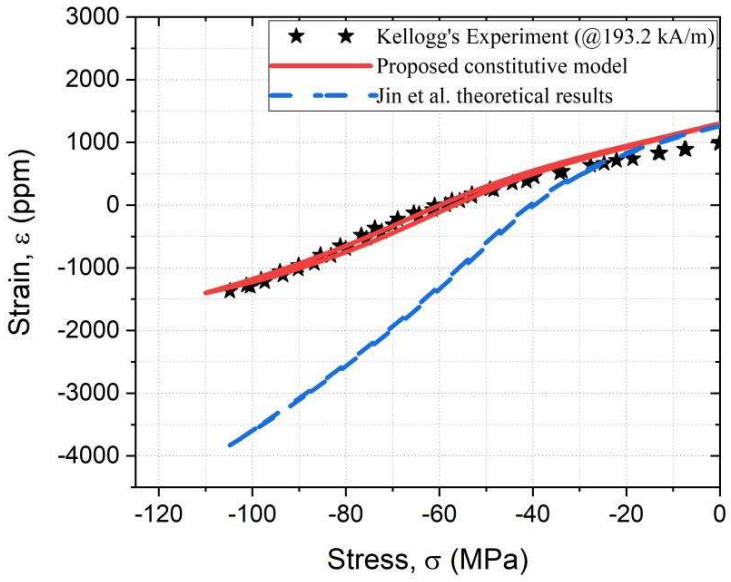

Figure 3.5: Comparison of compressive strain vs compressive stress curves predicted by the proposed constitutive model and Jin et al. model[54] with Kellogg et al. experimental results[17] (H=193.2 kA/m) at room temperature

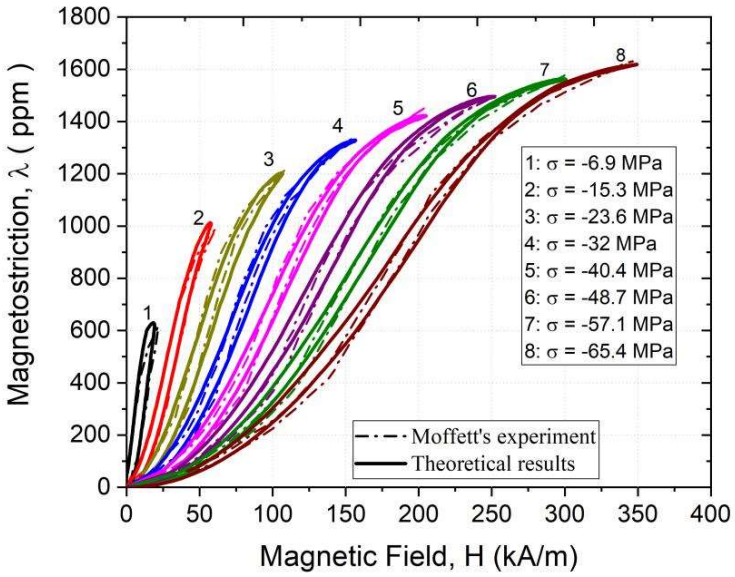

Figure 3.6: Comparison of the Magnetostriction hysteresis curves predicted by the proposed constitutive model under different pre-stresses with Moffett's experimental results[14] at room temperature.

Next, we validate the Moffett et al. experimental results[14] with the theoretical predictions for hysteretic curves at room temperature $T = 20\,℃$ under different pre-stresses. The material parameters are calibrated from the experimental investigation reported by Moffett et al[14]. Thus, the optimized material properties for the hysteretic constitutive model are listed in **Table 3-2**. **Figure 3.6** shows the comparisons between magnetostriction hysteresis loops predicted by the proposed constitutive model and the Moffett's experimental results[14] for different pre-stresses. It is evident from **Figure 3.6** that predicted magnetostriction hysteresis loops show well agreement (1.05% average error) with experimental results under different compressive pre-stress levels in all regions of the magnetic field.

The effect of the contribution of the Weiss's molecular field interaction energy between the domains within Terfenol-D (magnetostrictive material) can be analyzed by plotting magnetostriction hysteresis loops without considering the effect of Weiss molecular field

coefficient as shown in **Figure 3.7**. It is observed that the predictions of magnetostriction hysteresis loops are significantly lower than the experimental curves at low pre-stresses compared with the predictions at the high pre-stresses, where stress anisotropy dominates. Thus, the influence of Weiss's molecular field interaction energy must be included in the constitutive model of magnetostrictive material to quantify the material properties accurately.

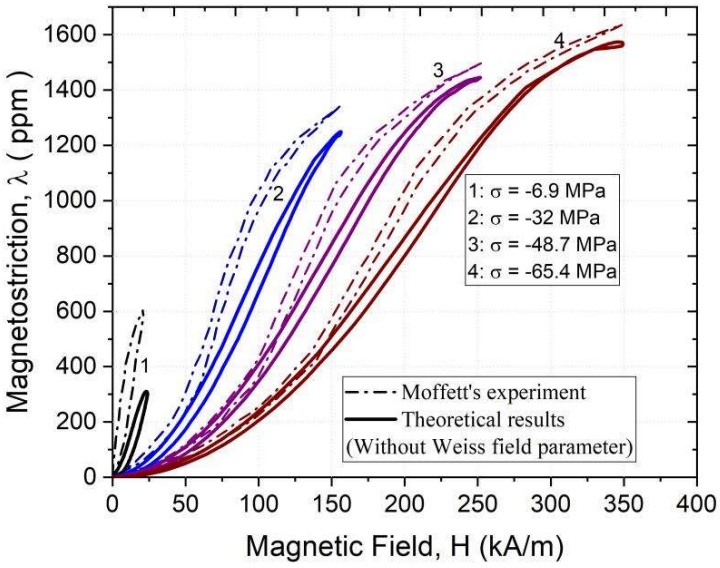

Figure 3.7: Comparison of the Magnetostriction hysteresis curves predicted by the proposed constitutive model without considering the Weiss filed parameter under different pre-stresses with Moffett et al. experimental results[14] at room temperature.

As well, the piezomagnetic coefficient $(d_{33} = \partial\varepsilon(\sigma, H)/\partial H)$ exclusively rely on the variations of the stresses and applied magnetic field. **Figure 3.8** shows the variation of d_{33} with the applied magnetic field and stresses. It demonstrate that in the region of low to moderate applied magnetic field, the piezomagnetic coefficient varies nonlinearly with applied magnetic field and prestress [14]. At high magnetic field levels, saturation occurs and the piezomagnetic coefficient becomes independent of applied magnetic field and prestress. Thus the present nonlinear constitutive model can accurately predict the

piezomagnetic coefficient in all regions of magnetic field, particularly in the region of low to moderate magnetic field.

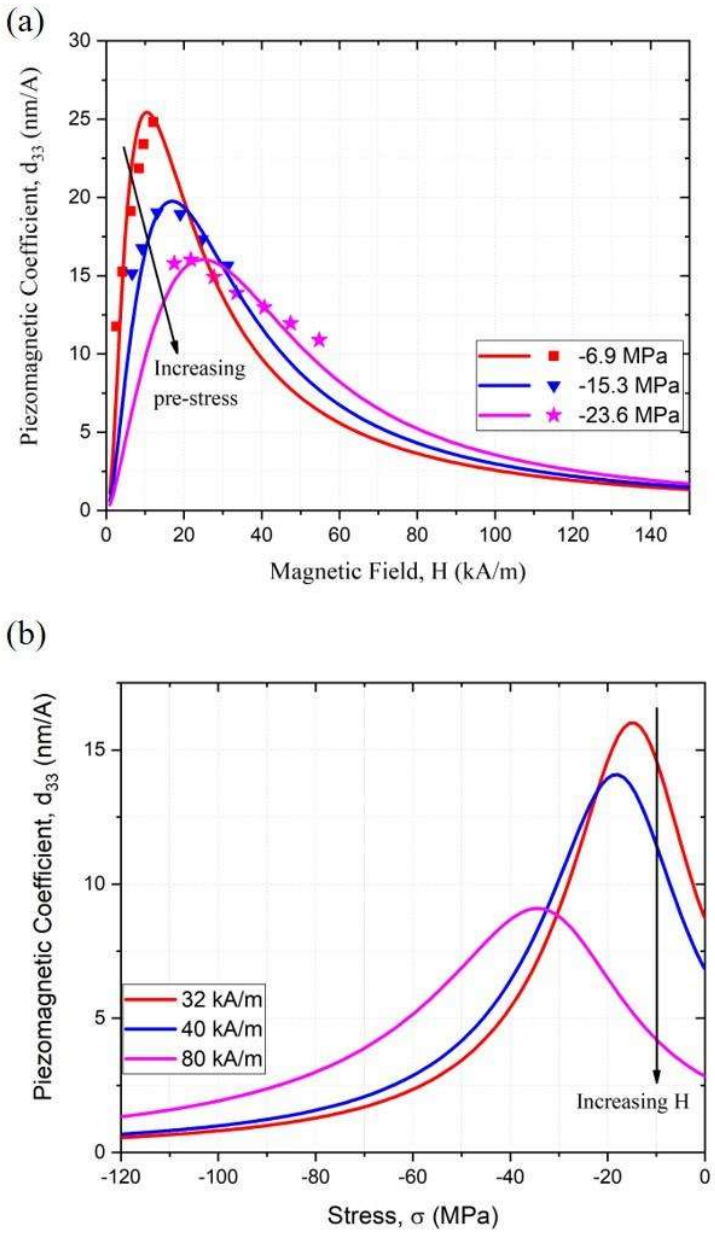

Figure 3.8 (a) Piezomagnetic coefficient vs magnetic field under various prestress (Scatters: Moffett et al. experimental results [14] ; solid lines: theoretical predictions) **(b)** Piezomagnetic coefficient vs compressive stress under different magnetic field levels.

Figure 3.9 (a) and **Figure 3.9 (b)** shows the magnetization and magnetostriction hysteresis curves generated by the constitutive model for different prestresses at room temperature when magnetic field approaches to saturation. It can be seen from **Figure 3.9 (a)** that the magnetization hysteresis curves under various pre-stress levels increases nonlinearly with the increase in the applied magnetic field and ultimately tend to saturation magnetization $M_s(T)$ for any value of pre-stresses. However, in the low and moderate applied magnetic field region, it is observed that steepness of the magnetization hysteresis curves decreases with the increase in compressive pre-stresses. This phenomenon can be explained, from the viewpoint of domain rotation, as an applied compressive pre-stress align the domains in a plane at right angles to the axial direction and consequently made the magnetization process more strenuous. Hence, high enough applied magnetic field needed to rotate all the domains in the axial direction to magnetize the material up to saturation. The magnetostriction hysteresis curve for a pre-stress level, as shown in **Figure 3.9 (b)**, increases with an increment in the applied magnetic field and reaches saturation at high enough applied field. The slope of magnetostriction hysteresis curves flattens with the increasing compressive pre-stress levels, hence possesses similar behaviour as magnetization hysteresis curves in low and moderate applied magnetic field regions. Furthermore, it exhibits entirely opposite behaviour in high regions of the applied magnetic field and achieves the higher saturation value ($\lambda_{max} = 3\lambda_s/2$ when $\sigma \to -\infty$) which is greater than the saturation magnetostriction coefficient λ_s. These predicted results by the proposed constitutive model are consistent with observed experimental results [5,14], which ensures the validity and reliability of magneto-elastic coupled hysteresis constitutive model.

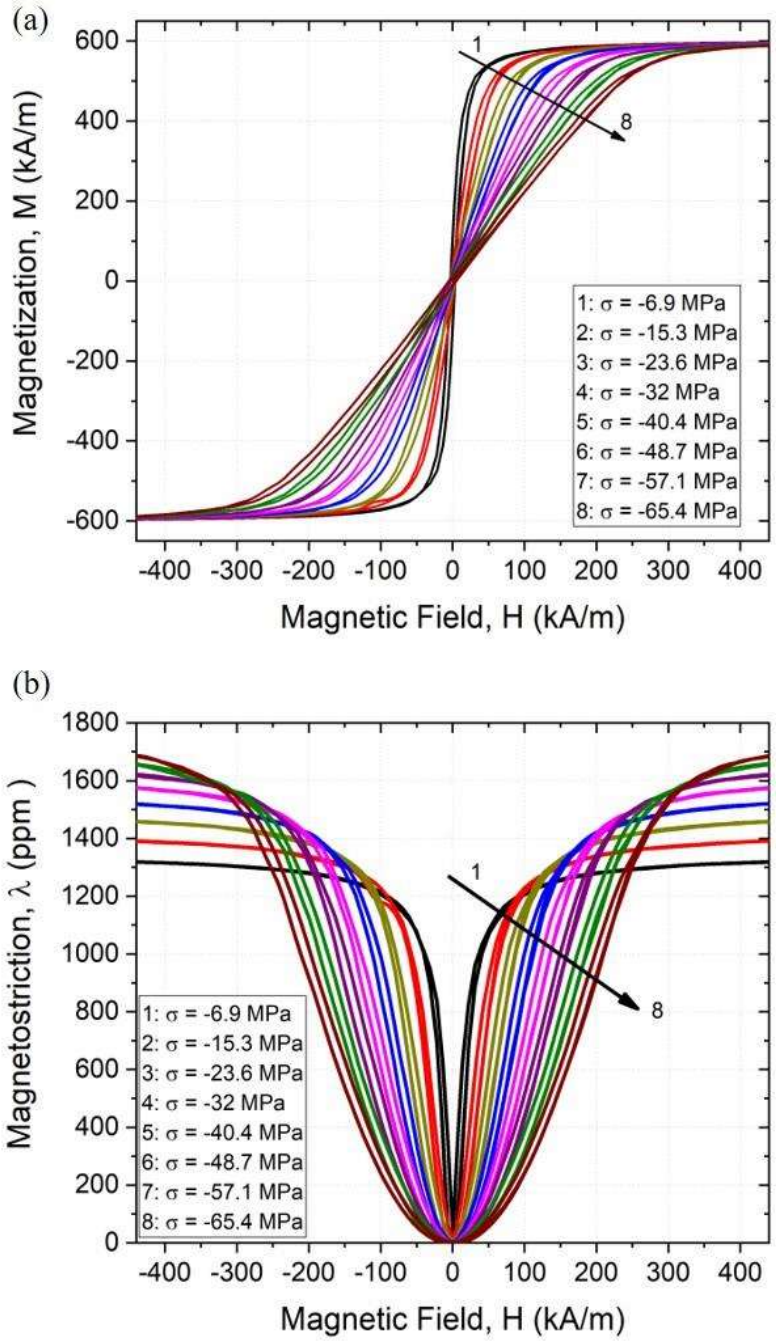

Figure 3.9: Magnetization and Magnetostriction hysteresis curves predicted by the proposed constitutive model under different pre-stresses at room temperature up to saturation **(a)** magnetization vs. applied magnetic field **(b)** magnetostriction vs applied field

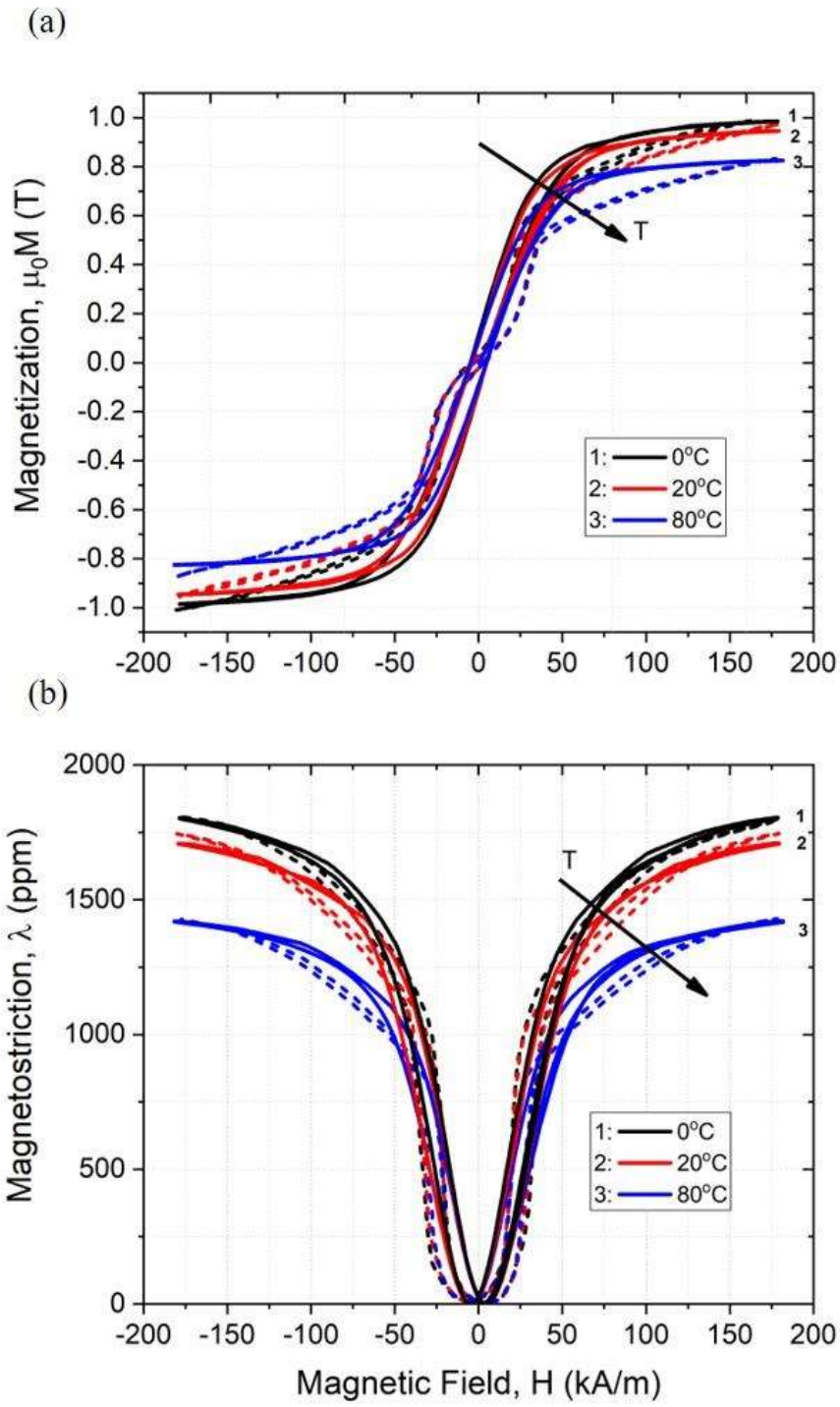

Figure 3.10: Comparison of the Magnetization and Magnetostriction hysteresis curves predicted by the proposed constitutive model under various ambient temperatures with Clark et al. experimental results[13] at 13.3 MPa compressive pre-stress. (Dashed lines: experimental curves; solid lines: theoretical predictions)

The effect of ambient temperature on magnetization and magnetostriction hysteresis curves are shown in **Figure 3.10 (a)** and **Figure 3.10 (b)** respectively. Here, magnetization and magnetostriction hysteresis curves measured by Clark et al.[13] under various temperatures, when prestress is 13.3 MPa, are selected for comparisons with theoretical predictions. In this case, based on experimental hysteresis curves, the optimal parameter values can be selected as given in **Table 3-2**. From **Figure 3.10 (a)** and **Figure 3.10 (b)**, we can find that the predicted hysteresis curves for both magnetization and magnetostriction indicate the negligible influence of temperature in the region of weak field and remarkable monotonous decrement with the temperature rise in the region of strong magnetic field. This also corroborates synergistically with experimental hysteresis curves and excellent accuracy is achieved for both magnetization (average error 2.8%) and magnetostriction (average error 2.1%) curves. As shown in **Figure 3.10 (a)** and **(b)**, in single-crystalline Terfenol-D, initially with the increase in the applied magnetic field, a relatively minor change in the magnetization and magnetostriction is observed until a critical field is reached, then an abrupt change in magnetization and magnetostriction is observed, which can be reasoned to the magnetic moment jumps between two $\langle 111 \rangle$ easy directions. Due to this delayed jumping in low magnetic field region up to the critical magnetic field, the discrepancies are noted in **Figure 3.10**. However, the initial jumping in low magnetic field region is further rectified by increasing the degree of crystalline alignment in some improved preparation techniques with the state-of-art methods such as ETREMA Crystal Growth (ECG)[118]. The present model incorporates the novelty of this physics, and that has been reflected in the results, enhancing the accuracy of the response predictions. Also, the proposed constitutive model is derived for isotropic magnetostrictive material, and **Figure 3.10** is the validation of Clark's experimental magnetic hysteresis curves [13] for twinned single-crystalline

Terfenol-D (with formula $Tb_{0.3}Dy_{0.7}Fe_{1.9}$) with ⟨111⟩ easy magnetization axis prepared by free-standing zone method (FSZM).

From the perspective of magnetic domain structure, increment in temperature increases the thermal energy, which increases the angle of the precession of magnetic moments. This precession decreases the magnetization component along the magnetic field direction. However, it is observed from hysteresis curves that magnetostrictive material shows excellent thermal stability in the region of weak fields. Thus, this effect can be used to optimize and design the smart magnetostrictive devices. From the above analysis, it is evident that the proposed model can effectively capture the magneto-thermo-elastic coupling of hysteretic behavior.

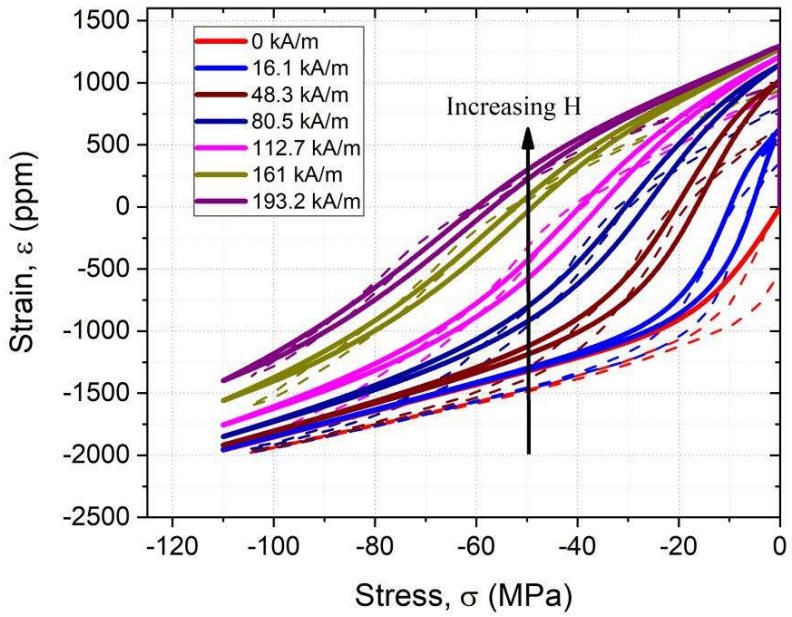

Figure 3.11: Comparison of compressive strain vs compressive stress curves predicted by the proposed constitutive model with Kellogg et al. experimental results[17] at room temperature (Dashed lines: experimental curves; solid lines: theoretical predictions)

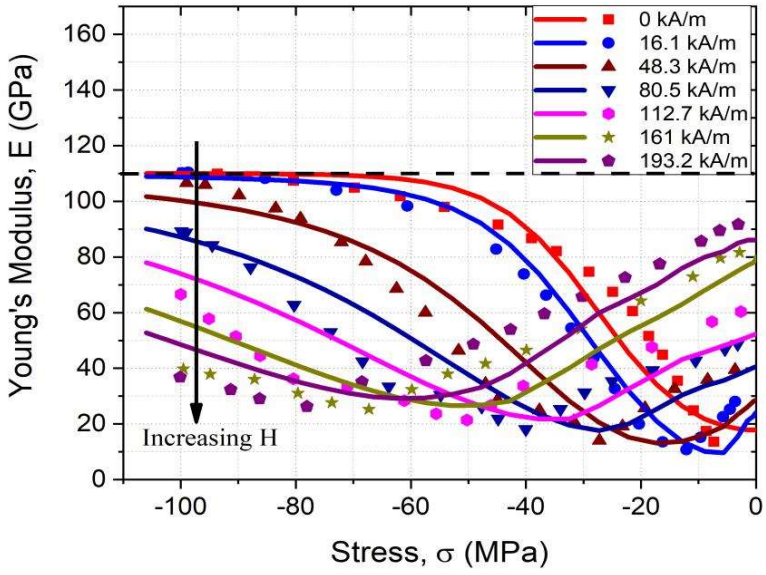

Figure 3.12: Comparison of Young's modulus vs compressive stress curves predicted by the proposed constitutive model with Kellogg et al. experimental results[17] under different magnetic fields levels at room temperature. (Scatters: experimental curves; solid lines: theoretical predictions)

Apart from effectively characterizing magnetostriction and magnetization hysteresis curves, Eqs. (3.29) and (3.30) are also able to predict the elastic properties under the coupled field environment. Hence, stress-strain hysteresis measurements reported by Kellogg et al.[17] are used to validate the proposed model at room temperature. The material constants are still selected the same such as those in **Figure 3.5**. The predicted results are plotted in **Figure 3.11**, along with the experimental curves. The stress-strain hysteresis curves estimated by the proposed constitutive model shows a good correlation with experimental data (average error 1.6 %) over the various magnetic fields. Further, **Figure 3.12** predicted the Young's modulus vs compressive stress curves under different magnetic fields and qualitatively consistent with Kellogg et al. experimental result[15,17]. It can be found, when the applied magnetic field is zero, the compressive strain vs compressive stress curve exhibits nonlinear nature with increasing compressive stress. Moreover, the calculated Young's modulus curves are gradually increasing to intrinsic Young's modulus at the magnetic saturation state

(E_{in}) with the increasing compressive stress. Further, the compressive strain vs. compressive stress curves under non-zero magnetic field exhibits higher nonlinearity and asymptotically approaches to zero applied field case with increasing compressive stresses where mechanical effects dominate the strain response. In this case, the predicted Young's modulus curves initially decrease from its stress-free state ($\sigma = 0$) value, then increases and finally approaches to intrinsic Young's modulus (E_{in}). It can also be seen that at stress free state ($\sigma = 0$) the value of Young's modulus increases with increasing magnetic field. The hysteresis is reduced at higher compressive stresses and lower applied field where elasticity response dominates the magnetic effects. There are some discrepancies arise in the predicted stress-strain results near the low magnetic field regime because in the proposed model mechanical hysteresis effects are not considered.

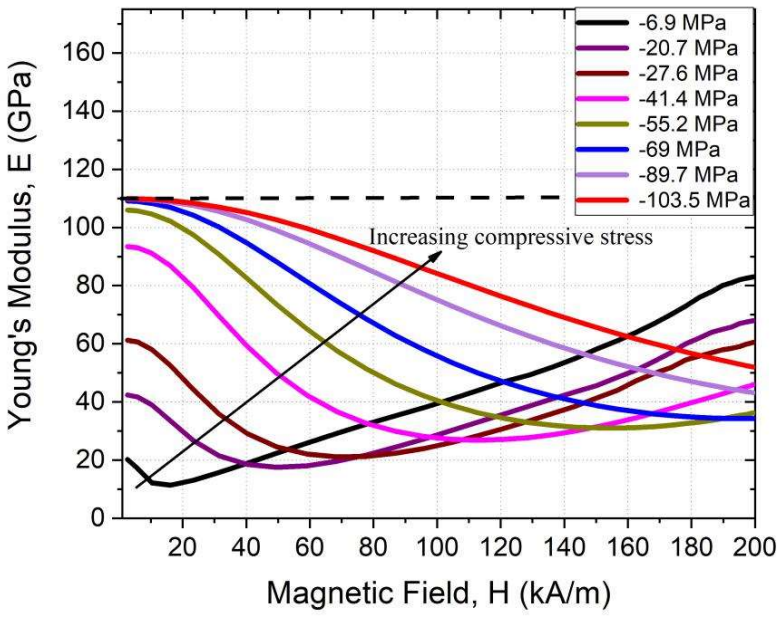

Figure 3.13: Predicted Young's modulus vs magnetic field curves under various compressive stresses at room temperature

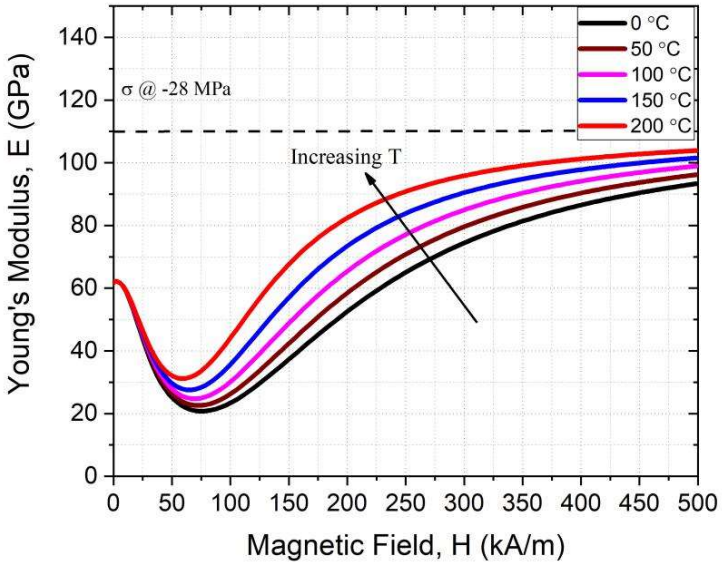

Figure 3.14: Predicted Young's modulus vs magnetic field curves under different temperatures at $\sigma = -28\ MPa$

The variation of Young's modulus is plotted against the magnetic field under different compressive stresses at room temperature (T = 20°C) in **Figure 3.13**. Comparing **Figure 3.12** and **Figure 3.13** it can be concluded that the Young's modulus approaches to saturation value (E_{in}) for greater compressive stress and weaker magnetic field or smaller compressive stress and stronger magnetic field. It can also be observed that under moderate compressive pre-stress and magnetic field, the material's Young's modulus adheres its minimum values around 15-30 GPa, i.e., much lower to saturation intrinsic Young's modulus (E_{in}). This range is almost consistent with the operating range of Terfenol-D rods[1] and so it is evident that the proposed constitutive model can reliably depict the ΔE effect. **Figure 3.14** represents the variation of Young's modulus with respect to magnetic field under different temperature levels at prestress level $\sigma = -28\ MPa$. From the illustration, it is found that the change in Young's modulus with temperature is negligible in weak magnetic field, but it increases significantly with temperature in strong field. This again reasserts the excellent thermal stability of magnetostrictive material in the region of weak fields. Thus, it can be concluded

that the Terfenol-D's compliance is characterized by the interaction between the mechanical and magnetic energy for a given applied magnetic field, temperature, and stress state. The predicted curves for Young's modulus under the effect of temperature, magnetic field and compressive stresses are qualitatively consistent with experimental results[15,17,119].

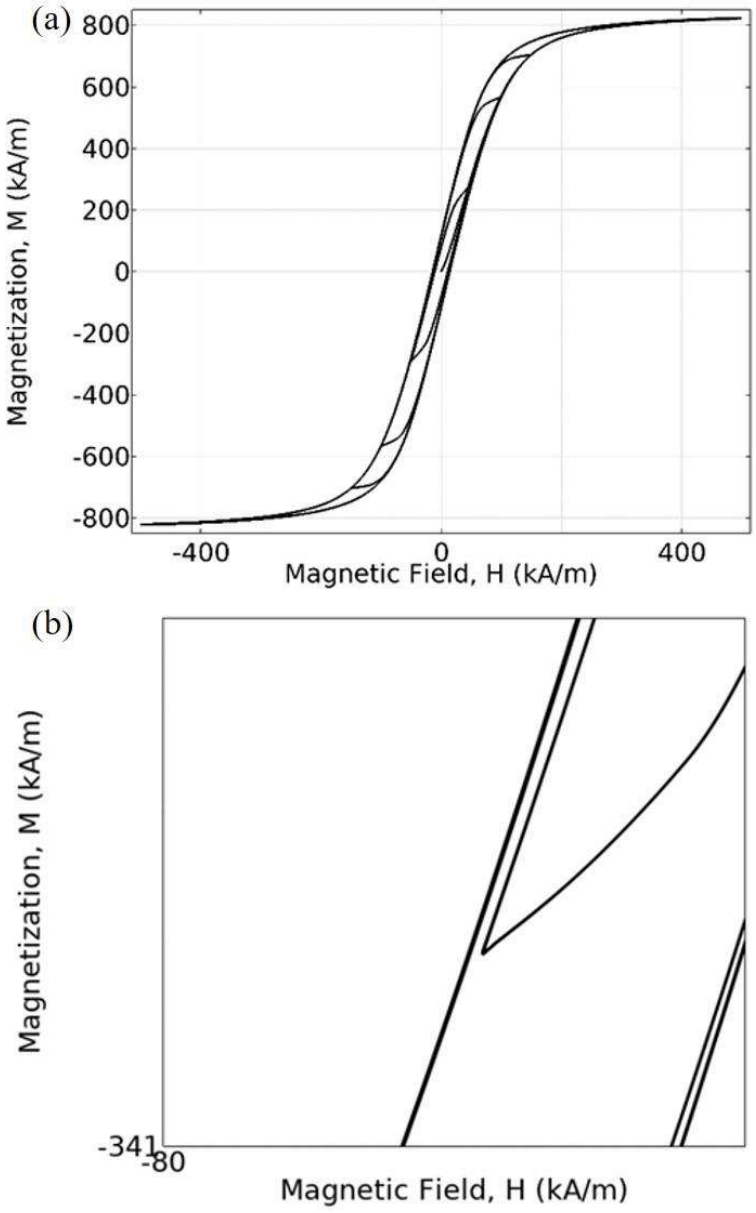

Figure 3.15: Predicted symmetric hysteresis inner loops for Magnetization vs Magnetic Field curves at $\sigma = -28\ MPa$ and room temperature **a)** inner hysteresis loops **b)** Zoomed view of the earmarked loop

Figure 3.15 demonstrates the calculated inner loops for magnetization vs magnetic field hysteresis curves obtained by cycling the magnetic field H with progressively decreasing magnitude. Arbitrary material parameters are taken as $M_s = 8.5 \times 10^5$ A/m, $\lambda_s = 1600$ ppm, $\sigma_s = 35$ MPa, $E_{in} = 110$ GPa, $\eta' = 0.06$, $T_c = 383.3$°C, $\beta = -5.6 \times 10^{-6}$ °C^{-1}, $\alpha = 12 \times 10^{-6}$ °C^{-1}, $c = 0.2$, $\chi_m = 19$ and $K = 20000$ A/m. It can be observed that the calculated inner loops show some discrepancies in loop closure (**Figure 3.15 b**). However, the difference is very small and in addition, for the giant magnetostrictive material, the hysteresis effects are not predominant in quasi-static and low frequency operating conditions and so the induced losses are insignificant. Therefore, the proposed vector model is efficient enough to capture the magneto elastic response of such material system. In addition to above discussion, the power converting devices can rise harmonic content in electrical systems and then to increase the hysteresis losses. The harmonic content in electrical systems along with the high frequency operating conditions, causes a distortion in the flux waveform deviating this from the sinusoidal one. This distorted flux waveform can add non-centered minor hysteresis loops (reversal curves) over the major hysteresis loops. The hysteresis models based on J-A model is only dependent on its previous time step value and the solution of its differential magnetization Eq. (3.41). There is no such evidence that confirm the return to initial point memory when non-saturated asymmetric loops or minor loops occurred. This discrepancy may be considered as a limitation of the proposed model and not well suited for calculation of reversal curves or minor loops. Some attempts [115–117,120] are being made to produce non-physical minor loops with classical J-A formulations, but all are limited to one dimensional applications. It is not look possible to apply these attempts directly to this proposed vector model. However, in case of quasi-static and low frequency operating conditions in sensors and actuators, the proposed model is fully capable of predicting the hysteretic nature of the magnetostrictive material.

3.6.2. Case Study 2: For magnetostrictive thin films

The Terfenol-D amorphous films experience frozen internal stresses while cooling the films from sputtering temperatures to room temperature during manufacturing. Those stresses arise due to the mismatch of thermal expansion coefficient between the base substrate and the deposited film layer. The so developed internal stresses can change the anisotropy energy of domains due to the magneto-elastic coupling effect and furthermore influence the magnetostriction and magnetic anisotropy of the Terfenol-D films [121–123]. The change in anisotropy energy alters the energy barrier that the domain wall requires to break away from the present pinning site and it moves irreversibly until it confronts another pinning site. Hence, the applied stress modifies the strength of pinning sites that inhibit the domain wall motion and as a consequence alters the pinning parameter K. For a material with positive magnetostriction (λ_s), pinning parameter decreases with tension but increases with compression and vice versa [51]. The initial susceptibility (χ_m) originating from rotation of the spins and domain wall motion also depends upon applied tensile and compressive stresses [49,124]. The experiments [47,125] detected a distinguishing characteristic of initial susceptibility (χ_m) of the positive magnetostrictive material, as χ_m decreases with increasing compressive stresses and increases with increasing tensile stresses from its zero stress state ($\sigma = 0$) value. Considering that the films have no internal defects, the geometric demagnetizing factor (N_{shape}) acts as a sole contributor to the demagnetizing factor (N). For a flat plate or film, the component of N_{shape} along magnetization direction approaches to zero when in-plane magnetic field applied and approaches to unity when out-plane magnetic field applied [58,126]. The value of N_{shape} is calculated from the approximate expression given in the existing study [60] and verified with the experimental study [16].

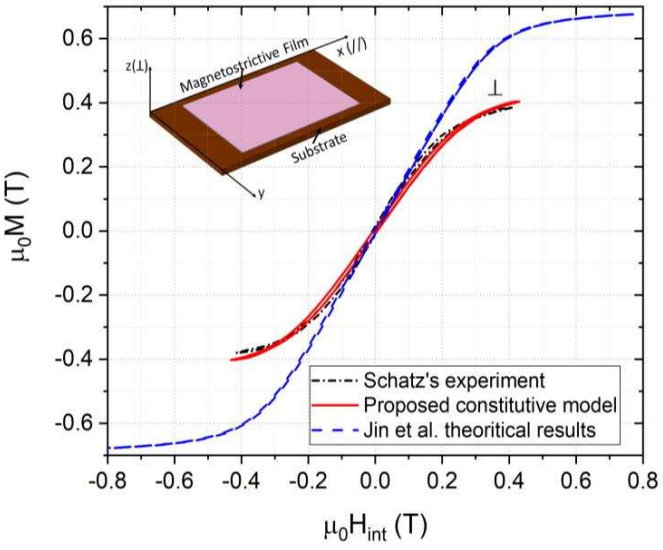

Figure 3.16: Comparison of predicted magnetization vs. internal magnetic field hysteresis curves by the proposed constitutive model and Jin et al. model [54] with Schatz's experimental results[16] for a film with in-plane tensile stress subjected to transverse magnetic field.

Table 3-3: Material Parameters of Terfenol-D amorphous films

Property	Tension	Compression
M_s $(\times 10^5$ A/m)	3.7	3.7
λ_s (ppm)	540	380
σ_s (MPa)	50	50
E_{in}(GPa)	50	50
η'	0.042	0.042
T_c (°C)	383.3	383.3
β $(\times 10^{-6}$ °C$^{-1})$	-2.8	-2.8
α $(\times 10^{-6}$ °C$^{-1})$	12	12
c	0.18	0.18
χ_m	5	3
K (A/m)	3000	10000
$N_{xx} = N_{yy}$	0.008	0
N_{zz}	1	0.87

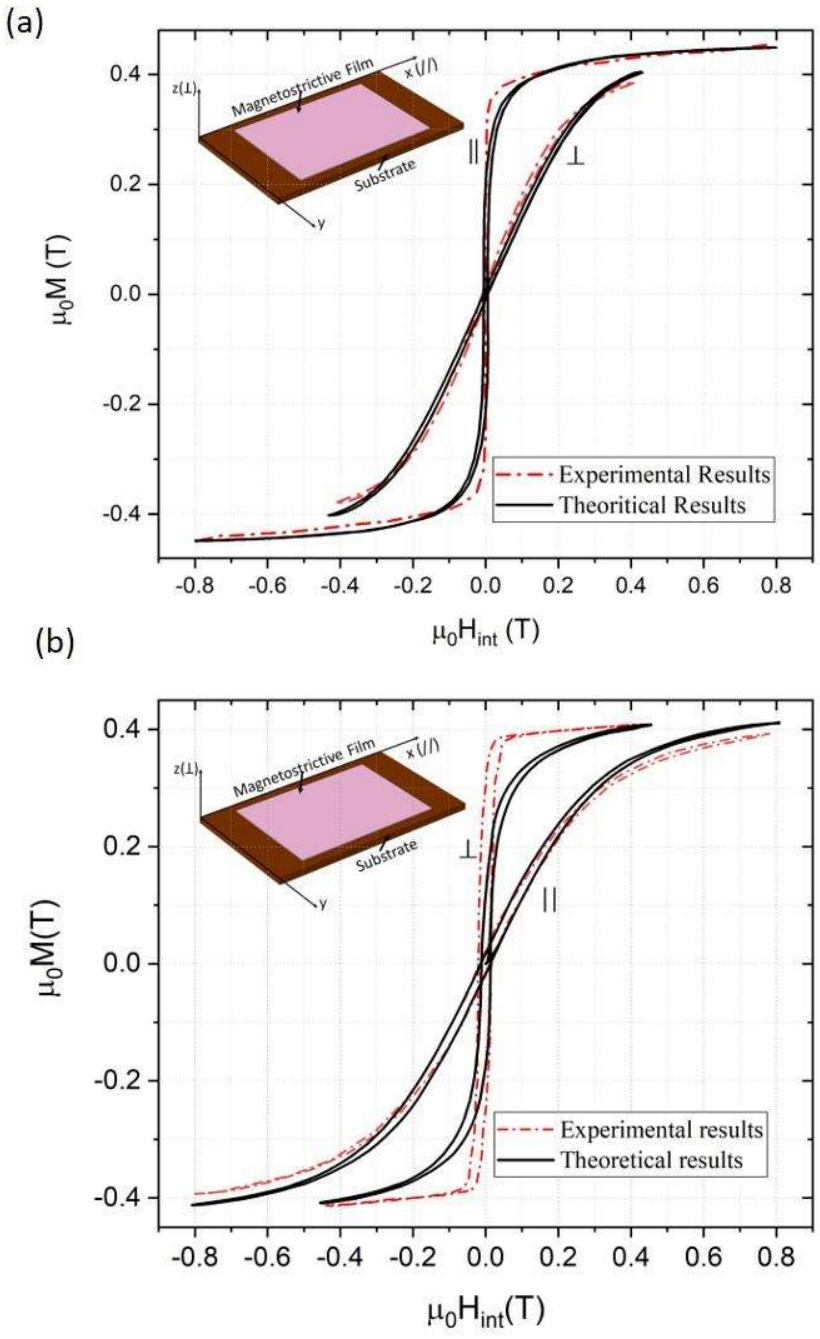

Figure 3.17: Comparison of predicted magnetization vs. internal magnetic field hysteresis curves with Schatz's experimental results[16] for a film under (a) tensile stress and (b) compressive stress at room temperature

Now for ensuring the multidimensional applicability, the proposed constitutive model and the phenomenological 3-D model introduced by Jin et al.[54] are used to simulate the Schatz

et al. experimental results [16] of Terfenol-D amorphous thin films at high prestress (greater than 100 MPa). Thus, based on the physical and experimental facts, the optimal parameters for the magnetostrictive films with tensile and compressive stress are summarized in Table 3-3. The same material parameters are retained as mentioned by Jin et al.[54] for the comparison purpose. **Figure 3.16** shows the results obtained from the present model and akin to the asymptotic nature of experimental delineations. The reflections are encouraging for two dimensional applications. The estimations from Jin et al.[54] model is nearly identical in the region of weak field and displays faster saturation phenomenon. This mismatch in the prediction of hysteresis curve at higher applied magnetic field is because of the linearization of the nonlinear part of elastic strain as well as the ignorance of the demagnetization effect in the earlier model. The inclusion of the demagnetization effect in present constitutive model causes to slow down the magnetization and magnetostriction saturation phenomenon. The effect of the demagnetization effect is discussed later in this section.

Next, as shown in **Figure 3.17** (a) and (b), the predicted hysteresis curves are coinciding well (1.26% average error for film under tensile stress and 2.3% average error for film under compressive stress) with the experimental hysteresis curves [16] for magnetostrictive thin films with frozen in-plane stresses that are subjected to a parallel magnetic field (i.e. along x-direction) or else a perpendicular magnetic field (i.e. along the z-direction). It is observed that the residual tensile stress in films induces in-plane magnetic anisotropy in which the easy direction of magnetization is parallel to the film plane and vice versa, the residual compressive stress in films induces perpendicular magnetic anisotropy where the easy direction of magnetization is perpendicular to the film plane. The change in magnetic anisotropy caused by internal stresses in positive magnetostrictive material can be explained on the basis of magnetic spin rotations. Specifically, a film with tensile stress tends to align

the spin distributions in the film plane whereas compressive stress tends to orient them perpendicular to the film plane. It can be predicted from Eq. (3.29) that the magnetostriction parallel to film plane ($\lambda_{x//}$) at high in-plane stress levels saturates at $\frac{3}{4}\lambda_s$ and $\frac{3}{2}\lambda_s$ for the spin distributions in the film plane and perpendicular to the film plane respectively, which is also consistent with the domain analysis.

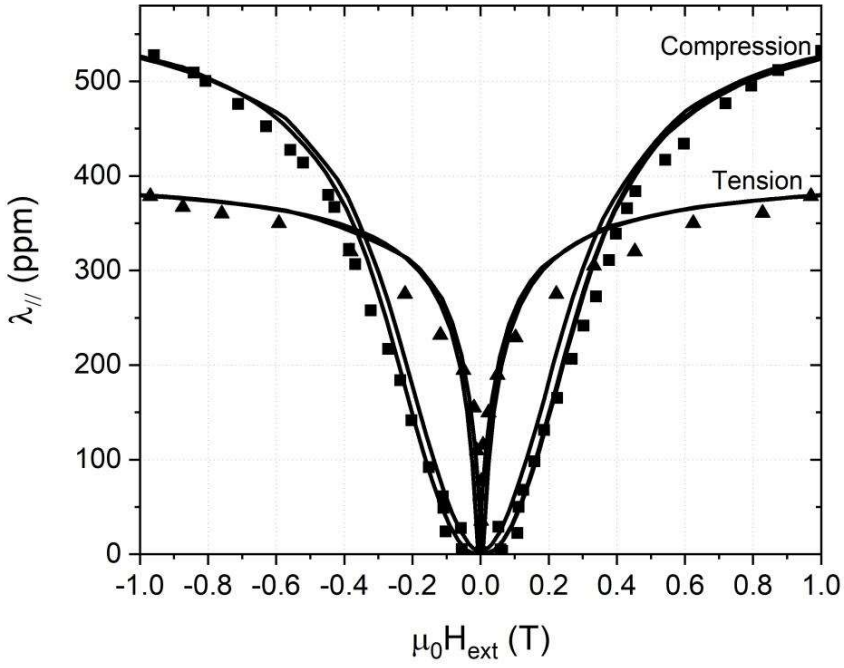

Figure 3.18: Comparison of predicted magnetostriction parallel to film plane vs. applied magnetic field hysteresis curves with Schatz's experimental results[16] for a film at room temperature.

Moreover, as shown in **Figure 3.18**, magnetostriction parallel to film plane reaches 400 ppm in case of tensile stress and achieves higher value 540 ppm in compressive stress case at applied magnetic field 1 T. As well as magnetostriction saturates much faster for the films with tensile stress than the films with compressive stress. Thus, the predicted magnetostriction vs applied magnetic field hysteresis curves also agree with the

experimental curves (2.1 % average error) for film under tensile stress and again ensures wider applicability of the proposed constitutive model.

The magnetostrictive film in the form of cantilever comprising of the film deposited on a non-magnetic substrate is considered as an example problem having wide application in the area of micro-actuation and sensing. To investigate the magneto-thermo-elastic characteristics of the magnetostrictive thin films thoroughly, hysteresis curves are produced using the same material parameters as described in **Figure 3.17**.

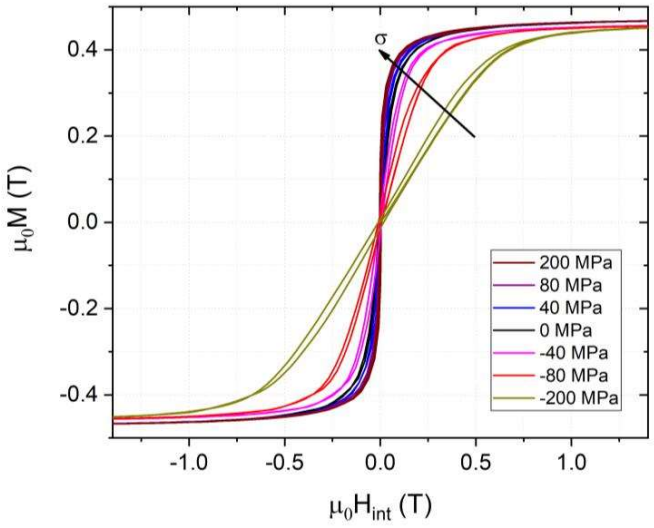

Figure 3.19: Predicted magnetization vs. internal magnetic field hysteresis curves at different in-plane stress levels, when subjected to in-plane applied field

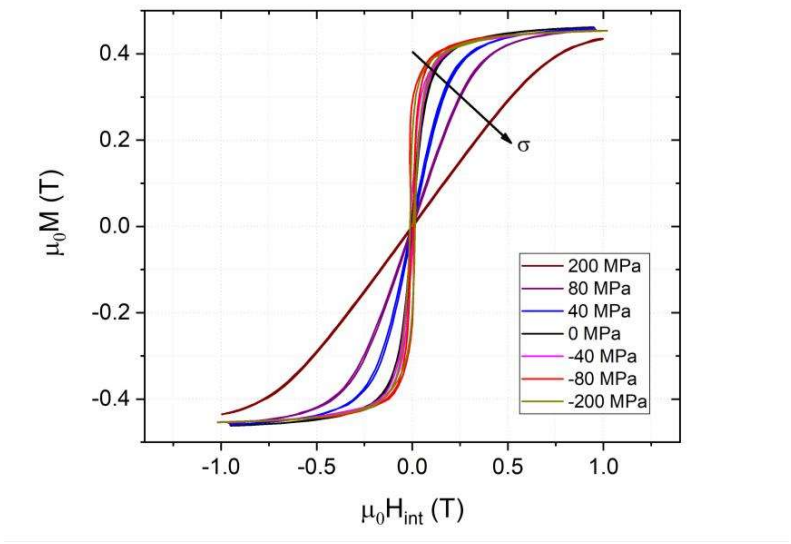

Figure 3.20: Predicted magnetization vs. internal magnetic field (hysteresis curves at different in-plane stress levels, when subjected to transverse applied field.

Magnetization hysteresis curves at room temperature are plotted at various in-plane stress levels in **Figure 3.19** and **Figure 3.20**, when magnetic field applied in-plane and transverse direction, respectively. It is conspicuous from the distribution pattern that the coercivity of hysteresis curves displays in-plane stress dependence and increases with in-plane compressive stresses. In-plane magnetization reaches saturation magnetization faster with increasing tensile stresses and slower with increasing compressive stress. In retrospect, for transverse magnetization, the entirely opposite phenomenon is observed.

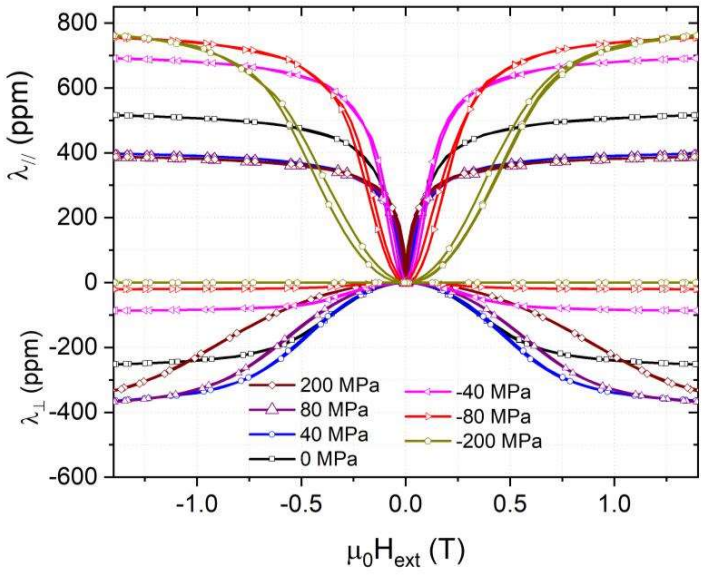

Figure 3.21: Predicted magnetostriction parallel to film plane vs. applied magnetic field hysteresis curves at different in-plane stress levels

Figure 3.21 illustrates the effect of in-plane stresses on magnetostriction parallel to the film plane at room temperature for both cases when the magnetic field applied in-plane ($\lambda_{//}$) and transverse direction ($\lambda_{\perp}$). It can be observed that $\lambda_{//}$ with increasing compressive stresses, initially decreases in the region of weak magnetic fields and then increases to $\frac{3}{2}\lambda_s$ in the region of strong fields. In case of increasing tensile stresses, $\lambda_{//}$ decreases to $\frac{3}{4}\lambda_s$ with increasing applied field and displays very low hysteresis. Further, it can be seen that $\lambda_{\perp}$ is a negative strain and decreases with increasing compressive stress to zero owing to the fact that all the spins are oriented parallel to the applied magnetic field. The value of $\lambda_{\perp}$ with increasing tensile stresses initially decreases in the region of weak magnetic fields and then increases to $\frac{3}{4}\lambda_s$ in the region of strong fields due to the isotropic spin distribution.

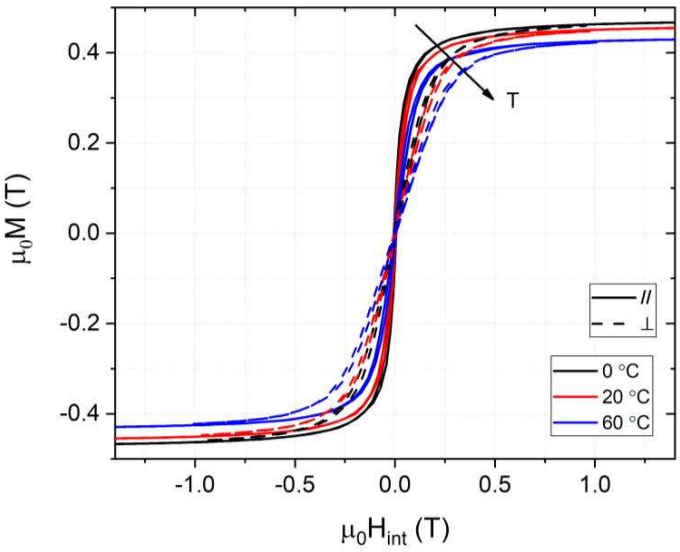

Figure 3.22: Predicted magnetization vs. internal magnetic field hysteresis curves at different temperatures (Solid lines: for in-plane applied field; Dashed lines: for transverse applied field)

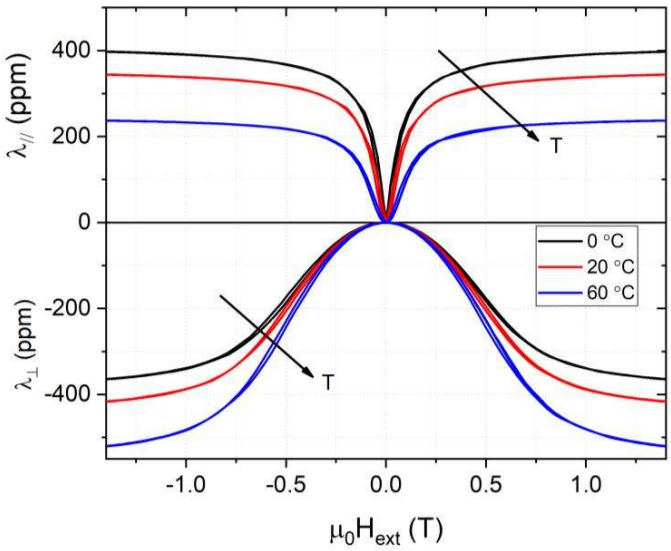

Figure 3.23: Predicted magnetostriction parallel to film plane vs applied magnetic field hysteresis curves at different temperatures

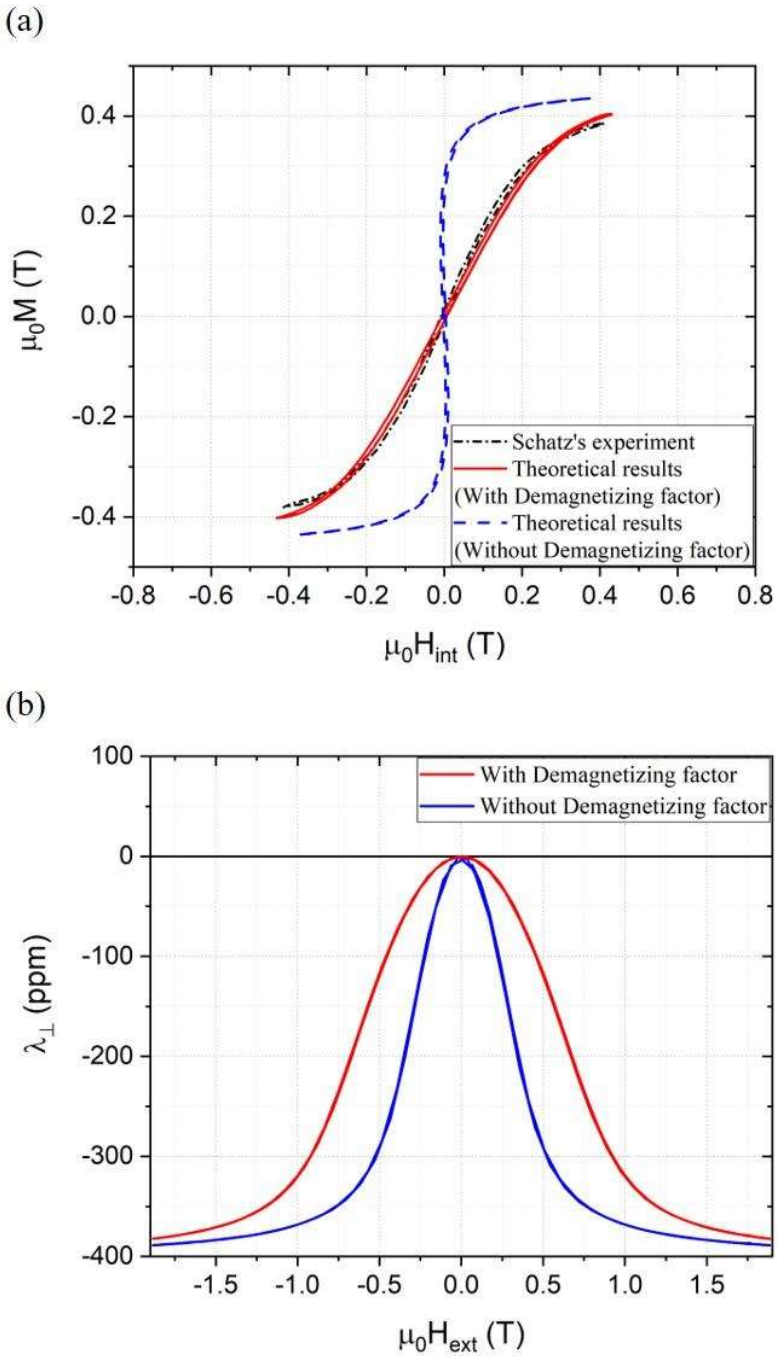

Figure 3.24: Effect of demagnetization factor on **(a)** magnetization vs. internal magnetic field hysteresis curves with Schatz's experimental results [16] **(b)** magnetostrictive strain vs. applied magnetic field curves for a film with in-plane tensile stress subjected to transverse magnetic field at room temperature.

Figure 3.22 and **Figure 3.23** illustrates the predicted hysteresis curves under various temperatures at 40 MPa in-plane tensile stress. Similar to the unidirectional case discussed earlier, both magnetization and magnetostriction curves indicates the negligible influence of temperature in the region of weak field and quickly fall with the further increment in the applied field. Hence, when the films are subjected to the higher magnetic field, the saturation magnetization and magnetostriction $\lambda_{//}$ decreases with increment in ambient temperature, whereas the negative magnetostriction $\lambda_{\perp}$ displays incremental behaviour.

In real field applications, the effect of demagnetization should be taken into account because as the surface divergence of magnetization vector rises the demagnetizing field [56,57], the magnetization distribution in non-ellipsoidal shapes [58–60] (such as bars, films) is no longer uniform and thereby, affecting the operation of magnetostrictive devices. Moreover, it is necessary to include the effect of demagnetization sources (such as stress concentration zones, fatigue cracks, voids etc.) in highly brittle magnetostrictive materials because these are inevitably generated in the actual field applications of the magnetostrictive devices. **Figure 3.24** displays the prediction results of some magneto-elastic response with (demagnetization factor N_{zz} =1) and without considering the contribution of demagnetization energy. It can be acknowledged from **Figure 3.24 (a)** and **(b)** that in comparison to zero demanganization factor case, with the increase in demagnetization factor, the magnetization and the magnetostrictive strain adapt more slow approach to reach the saturation value. The saturation value though does not change but attains at higher applied field. From domain point of view, as the demagnetizing energy increases, the magnetization and the magnetostriction approach slows down due to the domain wall motion and domain rotation gets weaker. These comparisons also convince that the demagnetization factor has a substantial impact on the magneto-elastic response of the magnetostrictive material.

Therefore, three dimensional models should consider invoking the demagnetization formulation to the magneto-thermos-elastic response characteristics.

3.7. Summary

A generalized coupled field vector model is developed to study the magneto-thermo-elastic response with applicability to 1D, 2D and 3D domain of giant magnetostrictive materials (GMM). The nonlinear hysteretic constitutive descriptions are based on the sound thermodynamic theory incorporating the coupling in three dimensions. The material constants associated with the proposed model can be calibrated from physical and experimental evidence. The constitutive relations are derived for bulk magnetostrictive materials of arbitrary shape and size, such as films and rods. Finite element based numerical simulations are carried out to assess the hysteretic magnetostriction and magnetization responses efficiently under the effect of a wide range of prestress and ambient temperature. The proposed model is generalized by incorporating a novel vector function of the hyperbolic tangent to accommodate the nonlinear elastic strain, which is built on the knowledge of isotropic elasticity theory and the physical facts of volumetric strain due to magnetostriction. A vector generalization approach for the J-A model to three dimensions is used for capturing the magnetic hysteresis that arises due to the pinning of magnetic domain walls.

The results of the theoretical model have been compared in certain cases with available experimental literature for the giant magnetostrictive material Terfenol-D, and the variations are consistent enough to validate the model. The observed asymmetries of the hysteretic magnetization, magnetostriction and stress vs. strain curves are critically analysed, citing the physics of magneto-elastic material. Also, the influence of demagnetization for field problems have been discussed and are of relevance for investigating the effect of demagnetization sources. The constitutive descriptions are found to describe qualitatively

and quantitatively the inherent vectorial hysteretic nature, stress anisotropies for a wide range of prestress levels, temperature effects and the variability in Young's modulus (ΔE effect). The average normalized root mean square error and the maximum errors are found to be within the range of [1.05 to 2.8] and [2.3 to 7.6], respectively. The discrepancies in inner loops as shown in **Figure 3.15** for the case of giant magnetostrictive material with quasi-static and low frequency operation is found to be small enough to affect the response characteristics. In the light of above demonstration with the observations presented, this might lead to future work with full scale implementation of reversal curves to the proposed nonlinear vector hysteresis model. The asymmetries of predicted results also indicate the significance of considering the effect of demagnetizing field and the Weiss molecular field on the nonlinear characteristics of magnetostrictive materials and gives a sound basis to explain the uncertainties and discrepancies of the response characteristics for the design and development of magnetostrictive smart devices.

This Page is Intentionally Left Blank